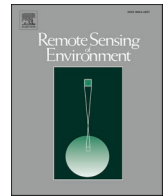# Vegetation moisture estimation in the Western United States using radiometer-radar-lidar synergy

David Chaparro, Thomas Jagdhuber, María Piles, François Jonard, Anke Fluhrer, Mercè Vall-llossera, Adriano Camps, Carlos López-Martínez, Roberto Fernández-Morán, Martin Baur, Andrew F. Feldman, Anita Fink, Dara Entekhabi

Vegetation moisture estimation in the Western United States using radiometer-radar-lidar synergy

David Chaparro [a,*], Thomas Jagdhuber [a,b], María Piles [c], François Jonard [d], Anke Fluhrer [a,b], Mercè Vall-llossera [e], Adriano Camps [e,f], Carlos López-Martínez [e], Roberto Fernández-Morán [c], Martin Baur [g], Andrew F. Feldman [h,i], Anita Fink [a], Dara Entekhabi [j]

[a] German Aerospace Center, Microwaves and Radar Institute, Münchener Strasse 20, 82234 Wessling, Germany
[b] Institute of Geography, University of Augsburg, Alter Postweg 118, 86159 Augsburg, Germany
[c] Image Processing Lab, Universitat de València, 46980 València, Spain
[d] Earth Observation and Ecosystem Modelling Laboratory, SPHERES Research Unit, Université de Liège (ULiege), Allée du Six Août 19, 4000 Liège, Belgium
[e] CommSensLab, Dept. of Signal Theory and Communications, Universitat Politècnica de Catalunya (UPC), Institut d'Estudis Espacials de Catalunya (IEEC), 08034 Barcelona, Spain
[f] UAE University, Al Ain, Abu Dhabi, United Arab Emirates
[g] University of Cambridge, Department of Geography, Downing Place, CB2 3EN Cambridge, UK
[h] Biospheric Sciences Laboratory, NASA Goddard Space Flight Center, Greenbelt, MD 20771, USA
[i] Earth System Science Interdisciplinary Center, University of Maryland, College Park, MD 20742, USA
[j] Civil and Environmental Engineering, Massachusetts Institute of Technology, Cambridge, MA 02139, USA

ARTICLE INFO

ABSTRACT

Monitoring vegetation moisture conditions is paramount to better understand and assess drought impacts on vegetation, enhance crop yield predictions, and improve ecosystem models. Passive microwave remote sensing allows retrievals of the vegetation optical depth (VOD; [unitless]), which is directly proportional to the vegetation water content (VWC; in units of water mass per unit area [kg/m^2]). However, VWC is largely dependent on the dry biomass and structure imprints on the VOD signal. Previously, statistical models have been used to isolate the water component from the biomass and structure components. Physically-based approaches have not yet been proposed for this goal. In this study, we present a multi-sensor semi-physical approach to retrieve the vegetation moisture from the VOD and express it as Live Fuel Moisture Content (LFMC [%]; the percentage of water mass per dry biomass unit). The study is performed in the western United States for the period April 2015 – December 2018. There, in situ LFMC samples are available for assessment. We rely on a VOD model based on vegetation height data from GEDI/Sentinel-2 and radar backscatter from Sentinel-1, which account for the biomass and structure components. Vegetation moisture is retrieved at L-, X- and Ku-bands by minimizing the difference between the modeled VOD and the VOD estimates from SMAP (L-band) and AMSR-2 (X- and Ku-band) satellites. Results show that the LFMC retrievals are independent of canopy height, land cover, and radar backscatter, demonstrating the capability of the proposed algorithm to separate water dynamics from the biomass/structure component in VOD. LFMC estimates at X- and Ku-bands reproduce well the expected spatiotemporal dynamics of in situ LFMC. Results show good agreement with in situ at a regional scale, with Pearson's correlations (r) between in situ LFMC samples and LFMC estimates of 0.64 (Ku-band), 0.60 (X-band) and 0.47 (L-band). Similar results are obtained independently for shrub and forest sites at X- and Ku-bands. In most comparisons between in situ and estimated LFMC, biases are below 10% of the dynamic range of LFMC. Performance at L-band is limited by the fact that this frequency senses the full vertical extent of the canopy, while in situ samples are taken only from top of canopy leaves to which X- and Ku-bands are much more sensitive. More insight will be needed for grasslands ($r = 0.44$ at X-band) using time-dynamic canopy height data. Furthermore, a pixel-scale assessment is conducted, showing a good agreement in most sites ($r > 0.6$). The proposed method can be tailored to exploit the synergies of past (e.g., AMSR-E), current (e.g., AMSR-2) and future satellite sensors such as CIMR and ROSE-L for global vegetation moisture mapping at different canopy layers.

1. Introduction

Vegetation moisture dynamics are mainly driven by soil moisture through plant water uptake and by atmospheric vapor pressure through stomatal conductance (Jonard et al., 2022). Consequently, variations in the conditions of soil, plant, and atmosphere impact the water and energy fluxes, control plant water and carbon uptakes, and modulate the relationship between the water, carbon, and energy cycles (Gentine et al., 2019; Grossiord et al., 2020). In that sense, vegetation and soils are responsible for moistening the atmospheric boundary layer over land through evapotranspiration. This guides land-atmosphere interactions and feedbacks, and in the end impacts the strength and duration of weather extremes such as droughts (Miralles et al., 2019) and extreme rainfalls (Bohlinger et al., 2017). It plays a major role in regional precipitation patterns (Wright et al., 2017; Yu and Notaro, 2020), and regulates continental climate through moisture recycling (Zemp et al., 2014). In addition, drying trends in vegetation can lead to forest mortality episodes, which are increasing under climate change. This ends in a reduced capacity of forests to act as carbon sinks (Chaparro et al., 2016; Martinez-Vilalta et al., 2019). Moreover, vegetation moisture controls crop productivity (Rigden et al., 2020), and conditions fuel flammability and therefore fire ignition and propagation risks (Chuvieco et al., 2010).

In this context, monitoring the vegetation water content could be instrumental to a wide variety of applications. Global observations of vegetation water content have the potential to increase our understanding of vegetation responses to water stress (Konings et al., 2021). In particular, estimating the live fuel moisture content (LFMC; [% of mass of water/dry biomass]) is relevant for fire risk assessment, as this variable is related to the combustibility and inflammability of fuels, and thus to the spread and intensity of fires (Yebra et al., 2018). The LFMC is directly related to the gravimetric vegetation moisture (m_g; [kg water / kg fresh biomass]), which can be normalized between minimum and maximum values to assess the relative water content (RWC; [%]) of vegetation. The RWC is a good indicator of the risk of plant mortality (Martinez-Vilalta et al., 2019; Rao et al., 2019) and is related to the vegetation water potential, a key variable in plant physiology (Zweifel et al., 2001; Konings et al., 2019; Jagdhuber et al., 2022).

Recently, global and regional databases of *in situ* LFMC have been made available (Duché et al., 2017; Yebra et al., 2019). However, these databases are created from laborious manual destructive measurements and do not represent the variability of global ecosystems due to the sparseness in spatial sampling. Complementarily, Earth Observation satellites can provide unique operational information on vegetation properties from local to global scales. In this regard, vegetation indices based on optical and infrared frequencies have been related to LFMC, being informative of the hydric conditions of plants. For instance, Chuvieco et al. (2002) demonstrated the applicability of Landsat Thematic Mapper indices to estimate LFMC in Mediterranean grasslands and shrublands. Also, Chuvieco et al. (2004) showed that the combination of the Normalized Difference Vegetation Index (NDVI) with land surface temperature (LST) remote sensing data allows estimating LFMC over the same vegetation types. Importantly, several studies have applied infrared and optical data from the Moderate Resolution Imaging Spectroradiometer (MODIS) to derive LFMC at local (Yebra and Chuvieco, 2009), regional (Myoung et al., 2018, in Southern California), and continental scales (Yebra et al., 2018, in Australia). However, optically-derived vegetation indices are indirectly related to the hydric conditions of plants, unlike microwave sensors whose signal is directly related to the water content (Piles et al., 2011). Dennison et al. (2005) showed that the Normalized Difference Water Index (NDWI) outperforms NDVI when estimating LFMC because the former is linked to vegetation water content due to measurements in the water absorption bands in the infrared, while the latter is linked to chlorophyll content making use of reflectance measurements in the visible and infrared regions of the spectrum. Optical/infrared sensors have the advantage of providing information at high spatial resolution (meters). However, their measurements are masked by clouds, are limited by penetration capabilities (they sense only the top of the canopy leaves), cannot be obtained at night, and saturate for medium to high vegetation densities. Temporal samplings are weekly at best under cloud-free conditions.

In the last decades, passive microwave remote sensing has consolidated as a technique to provide all-weather soil moisture (SM; [$m^3 \cdot m^{-3}$]) and vegetation attenuation information worldwide every 2 to 3 days. At the cost of a coarse resolution of tens of kilometers, passive microwave sensors such as the Advanced Microwave Scanning Radiometer (AMSR; 2002–2003; Koike et al., 2000) on board of ADEOS-II, the Advanced Microwave Scanning Radiometer for EOS (AMSR-E; 2003–2011; Kawanishi et al., 2003) on board of the Aqua satellite, and, more recently, the satellites Soil Moisture and Ocean Salinity (SMOS, launched in 2009; Kerr et al., 2010), the Global Change Observation Mission (GCOM-W1, launched in 2012; Imaoka et al., 2010), and the Soil Moisture Active-Passive (SMAP, launched in 2015; Entekhabi et al., 2010), can monitor the land surface regardless of weather conditions, and sense different canopy and soil emission depths depending on the microwave frequency. The vegetation optical depth (VOD; [unitless]) is a microwave-derived parameter measuring the attenuation that the vegetation layer exerts over the soil and vegetation emissions in the microwave frequencies of the electromagnetic spectrum. The VOD depends on the water content, biomass, and structure of the vegetation (Jackson and Schmugge, 1991; Konings et al., 2019; Liu et al., 2015). Several studies have shown that it can be transformed into vegetation water content (VWC) in water mass per unit area [kg/m^2] (*e.g.*, Santi et al., 2017). However, this approach requires an empirically calibrated constant to establish the VOD-VWC linear relationship, and it is not informative on the real hydric status of vegetation due to its dependence on biomass (Jackson and Schmugge, 1991; Togliatti et al., 2019). Indeed, a larger VWC will systematically be found in dense vegetation (*e.g.*, forest) as compared to low vegetation (*e.g.*, grassland), just because more biomass stores more water per surface area.

In contrast, the estimation of LFMC has the advantage of being biomass independent. The application of microwave remote sensing to obtain LFMC has been explored in recent studies. Fan et al. (2018) derived soil moisture and vegetation indices from different microwave frequencies (C-, Ku-, K- and Ka-bands) to infer LFMC in the Mediterranean, and Jia et al. (2019) combined modeled and *in situ* air temperature data and SMAP SM for the same purpose in Southern California. Forkel et al. (2023) developed a set of regression models using VOD at C-, X- and Ku-bands, *in situ* LFMC (for calibration), and/or the leaf area index (LAI; [m^2/m^2]), to derive LFMC at a global scale between 2000 and 2017. They showed that, among these models, the one including LAI obtained the highest performance. Rao et al. (2020) demonstrated that LFMC estimates from optical data improved when Sentinel-1 radar backscatter was also included in the model. Importantly, the last two examples highlight the need to use information on the canopy structure/biomass component (*e.g.*, with LAI or radar backscatter) to isolate the water component from the VOD (Forkel et al., 2023; Rao et al., 2020). These studies also showed the potential of the synergistic use of microwave vegetation attenuation together with other remote sensing acquisition techniques to retrieve LFMC. Indeed, these synergies have led to the first global microwave-based LFMC product (Forkel et al., 2022).

Nevertheless, to our knowledge, an approach to the problem based on disentangling the water effect on the VOD signal using physical (*e.g.*, attenuation-based and dielectric) models is still poorly explored. In that sense, Grant et al. (2014) merged a canopy opacity model applicable at microwave frequencies with a vegetation dielectric model to retrieve gravimetric vegetation moisture (m_g; [kg_{water} / $kg_{wet\ biomass}$]) based on SMOS VOD data. Note that m_g can be transformed into LFMC with a simple computation (LFMC $= (m_g/(1-m_g)) \cdot 100$). Fink et al. (2018) developed an attenuation-based retrieval of m_g based on minimizing the difference between modeled and SMAP-based VOD data to derive the

best-fitting dielectric constant of vegetation which then was converted into m_g values using a dielectric model. This approach required the synergetic use of passive microwave VOD (from SMAP), LiDAR canopy vegetation height data (h_{veg}, [m]; from the Ice Cloud and land Elevation Satellite; ICE-Sat), and radar vegetation volume fraction information (δ, [m$^3 \cdot$m^{-3}]; a parameter proportional to radar vegetation indices and derived from the three months of SMAP L-band radar data available). The h_{veg} and δ parameters accounted for the biomass and structure of vegetation which are embedded in the VOD signal. The same approach was applied at the field scale by Meyer et al. (2019) to estimate m_g for a winter wheat field, in this case by using a tower-based radiometer for sensing the attenuation, *in situ* measurements of h_{veg}, and a set of simulated values of δ. Results indicated a strong agreement between *in situ* and estimated m_g ($r^2 = 0.89$).

Here, we propose a multi-sensor semi-physical algorithm which builds on Fink et al. (2018) to disentangle the water component (gravimetric vegetation moisture; m_g) from the VOD signal of SMAP and AMSR2. The algorithm minimizes the difference between the VOD data and a VOD model to retrieve m_g. The structure/biomass component in the VOD model is based on canopy height (h_{veg}) data from the Global Ecosystem Dynamics Investigation (GEDI) and on radar backscatter information from Sentinel-1. We convert the m_g retrievals to LFMC units for comparison with *in situ* data. Then, the goals of this paper are: (i) to retrieve LFMC in the Western United States and compare the results with *in situ* LFMC information; and (ii) to analyze the sensitivity of the LFMC estimates to the different VOD components (biomass, structure, and water), land cover types, permittivity mixing models, and microwave frequencies (L-, X- and Ku-bands).

2. Data and methods

2.1. Study area

The study area covers the entire Western United States ($-125°$W to $-99°$W, $47°$N to $29°$N). This region serves as a suitable testbed for our study as it maximizes the number of *in situ* samples and the diversity of land cover types for the assessment of the retrievals (see Section 2.2.4). The region includes forests in the West (temperate climate) and in the Rocky Mountains (colder and wet). In the South and central areas, short shrublands dominate the arid landscape of the Great Basin. The East of the study region is dominated by grasslands and a wet climate (Fig. S1).

2.2. Datasets

2.2.1. Vegetation optical depth

The vegetation optical depth (VOD; [unitless]) is used to minimize the difference with the VOD model in order to retrieve m_g (Section 2.3). VOD from three microwave frequencies (L-, X- and Ku-bands) is applied to compare results for different sensing depths through the canopy, which are deeper at lower frequencies (f, [GHz]). L-band VOD is known to be representative of the full canopy depth even in dense vegetation forests (Li et al., 2021; Bueso et al., 2023). In contrast, the sensing depth of X- and Ku-band VOD is limited to the layers within the top of the canopy, qualifying them for investigating the characteristics of short vegetation such as shrubs and grasses (Rodríguez-Fernández et al., 2018; Chaparro et al., 2019; Olivares-Cabello et al., 2022; Yang et al., 2023). The data availability of satellite-derived VOD defines the study period, ranging from April 2015 to December 2018.

L-band VOD (L-VOD; f = 1.4 GHz; λ = 21.4 cm) is retrieved from SMAP measurements using the Multi-Temporal Dual Channel Algorithm (Konings et al., 2016; Feldman et al., 2021). SMAP was launched in January 2015. It has a revisit time of 2 to 3 days in the study region and a native resolution of ~40 km. Here, SMAP data provided at the 9 km EASE2 grid is aggregated to 0.25° for consistency with the other VOD products. The X-band VOD (X-VOD; f = 10.65 GHz; λ = 2.8 cm) and the

Ku-band VOD (Ku-VOD; f = 18.7 GHz; λ = 1.6 cm) are obtained from the Advanced Microwave Scanning Radiometer 2 (AMSR-2) on board of the GCOM-W1 satellite, launched in May 2012. The product used for these two frequencies is the VOD Climate Archive (VOD-CA; Moesinger et al., 2020), and its data is available until December 2018 (X-VOD) and July 2017 (Ku-VOD). Therefore, note that the last months of the study period are not covered by the Ku-band. GCOM-W1 has a revisit time of 2 days and native spatial resolutions of 42 × 24 km (X-VOD) and 22 × 14 km (Ku-VOD). The product is provided at 0.25° gridding. The C-band VOD (f ~ 7 GHz; λ = 4.3 cm), while also available in the VOD-CA dataset, cannot be used in this region due to severe radio-frequency interferences (Moesinger et al., 2020).

All VOD datasets are processed as follows. First, they are screened for snow and frozen ground applying the ground freeze/thaw and snow flags from the SMAP level 3 soil moisture product (O'Neill et al., 2020). Second, pixels where standing water covers >5% of the pixel area are screened out. Water location is based on land cover data from the ESA-CCI (ESA, 2017). Both snow/frozen ground and land cover data are aggregated to the 0.25° common grid before screening. Third, for each pixel, VOD values greater/smaller than two standard deviations above/below the mean are considered outliers and are removed. In this step the VOD seasonality has been removed for the computation of outliers and then added again. Fourth, VOD is smoothed over time using an 11-day Gaussian time-moving window to remove short temporal variations which can be in part signal noise (Chaparro et al., 2022). The temporal window chosen is not incidental. A short window needs to be used to ensure we are not filtering out the high-frequency fluctuations of the water signal in VOD.

Fig. 1 shows the VOD datasets in terms of means and seasonal amplitudes for the entire study period (April 2015 to December 2018). Seasonal amplitude is the difference between maximum and minimum in the seasonality, which is computed first by averaging the VOD of all years daily, and then smoothing the result using a 45-day moving average. As expected, VOD from all frequencies is highest in forested regions, especially in the evergreen forests in the West and the North (see also Fig. S1a). However, less spatial contrast is found between forested and non-forested areas at Ku-VOD, which also has notably higher VOD mean values than X- and L-VOD (Fig. 1a, c, and e). Also, note that the seasonal amplitude increases with frequency, and that it is especially higher in the north and east areas (mainly grasslands and shrublands) at Ku-VOD (Fig. 1). Examples of VOD time series for main land cover types are shown in Fig. S1.

2.2.2. Radar backscatter

Radar backscatter data will be used to account for the structure/biomass component of VOD in the VOD model (Section 2.3). Backscatter at cross-polar (σ_{VH}; V: vertical polarization, H: horizontal polarization) and vertical (σ_{VV}) polarizations are obtained from the European Space Agency's (ESA) Sentinel-1 mission (Torres et al., 2012), operating at C-band (f = 5.4 GHz; λ = 5.9 cm). This mission comprises two satellites, Sentinel-1A (launched in April 2014) and Sentinel-1B (launched in April 2016 and ceased in August 2022). The revisit time with the two satellites was at least every six days anywhere on the globe until the Sentinel-1B failure. Nevertheless, in the specific study region of this work, the Sentinel-1 data availability is sparse until July 2016, and a revisit time of six days is not available until January 2017. This hampers the retrieval of continuous vegetation moisture time-series during part of the study period (April 2015 – July 2016). Still, this period is kept in the analyses since it matches the dates when more *in situ* data are available for comparison (see Section 2.2.4).

The Sentinel-1 σ_{VH} and σ_{VV} information is included within the SMAP/Sentinel-1 L2 radiometer/radar product (Das et al., 2019; Das et al., 2020), at 3-km gridding. This product includes median filters to remove returns from human-built structures and radar speckle. The radar data used in this product come exclusively from Sentinel-1. Data with acquisition angles <30° or >50° are removed because a
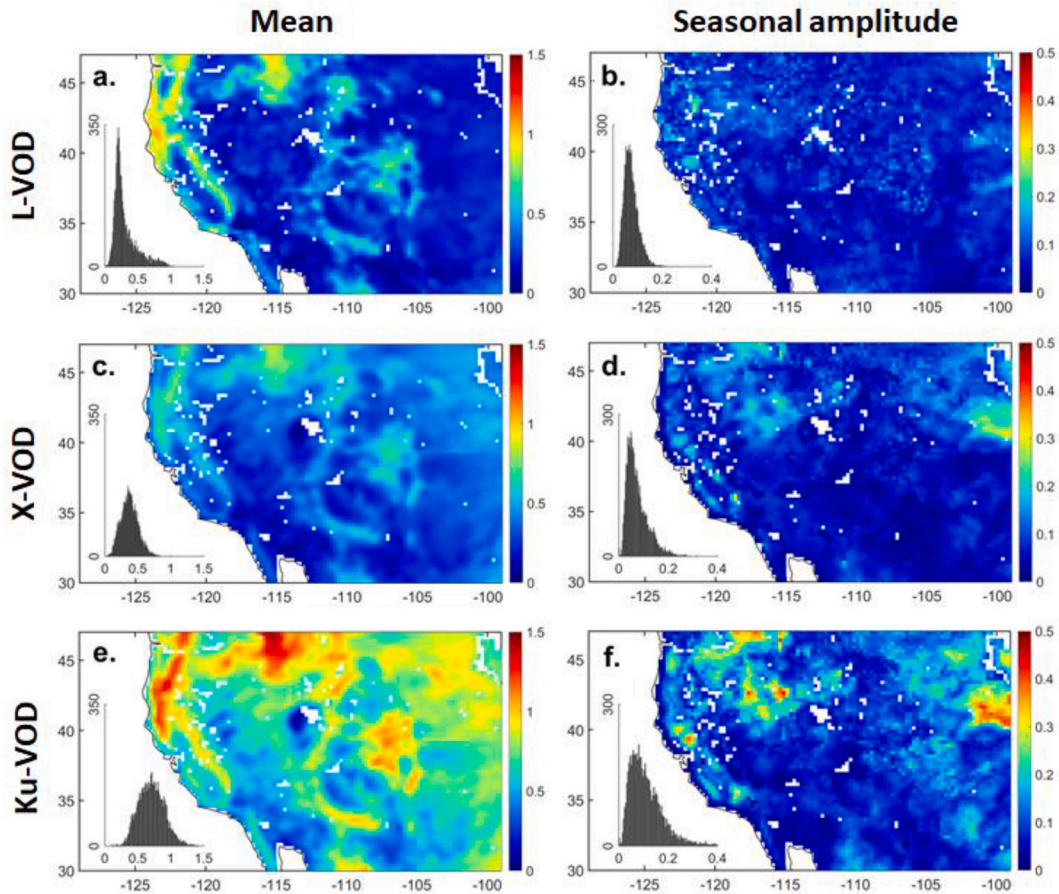
Fig. 1. Mean (left column) and seasonal amplitude (right column) of VOD for the study period (April 2015 – December 2018) in the western United States. Frequency bands are L-band (a, b), X-band (c, d), and Ku-band (e, f).

comparison of histograms using 5°-width angle bins shows that only data between 30° and 50° have similar distributions (not shown). Backscatter values <−30 dB are also excluded as they are considered as noise in terms of the noise equivalent sigma zero (NESZ) of Sentinel-1. All backscatter data are transformed from dB to linear units and screened for standing water (if it spans >5% of the pixel) and surface temperature (if it is <2.5 °C). After all filtering, 88% of the initial data remain.

The radar backscatter data are applied to compute a normalized cross-polarization backscatter (hereafter σ_{norm}), which is a simplification of the radar vegetation index (RVI) formula from Kim and van Zyl (2000). Both RVI and σ_{norm} are measures of volume scattering from randomly oriented dipoles and increase with more complex and dense vegetation (*i.e.*, when the vegetation layer contains complex structures involving leaves, branches, and trunks; Szigarski et al., 2018). The σ_{norm} is computed as follows (Mandal et al., 2020):

$$\sigma_{norm} = \frac{\sigma_{VH}}{\sigma_{VV} + \sigma_{VH}}, \tag{1}$$

where σ values are in linear units. Once σ_{norm} is computed, it is averaged to the 0.25° grid and smoothed in time using a Gaussian 61-day moving window.

Fig. 2(a and b) shows the mean and seasonal amplitude of σ_{norm}. The highest values correspond to forests, especially to those in temperate coastal areas. Forests and most shrublands show the lowest seasonal amplitudes, as expected due to their constant biomass, while high seasonal amplitudes are in the grasslands in the East (Fig. 2a and b). Seasonal amplitudes of σ_{norm} are computed like those of VOD. Example time-series of σ_{norm} are shown in Fig. S1d.

2.2.3. Vegetation canopy height

The Lidar-derived vegetation height (h_{veg}, [m]) data is also used to account for the structure/biomass component of VOD in the VOD modelling approach (Section 2.3). Data on h_{veg} is obtained from Lang et al. (2022). The authors fuse LiDAR data from the Global Ecosystems Dynamic Investigation (GEDI) with Sentinel-2 optical data, to train a deep learning model based on convolutional neural networks (CNN). This model yields retrievals of h_{veg} at 10 m spatial resolution worldwide for the year 2020. Also, an uncertainty map is computed by measuring the standard deviation of five independent CNNs (Std(h_{veg})) with the same structure as the original model, but different parameter weights (Lang et al., 2022).

Here, all data points with Std(h_{veg}) > h_{veg}/2 are considered unreliable and are removed. This accuracy filter works well in forests and mixed vegetation landscapes. Nevertheless, in the shortest shrubland areas (14% of pixels), the filter is too strict and the aggregated h_{veg} is finally equal to zero meters because the uncertainty screening has removed all values. The reason for this low accuracy is probably the poor capability of space-borne LiDARs to sense the absolute height of short vegetation. In the cases where all data were removed, the original values are restored and aggregated without considering uncertainty. This does not have a relevant impact on the final retrieval, because the uncertainty in these cases is very low in absolute terms (95% of the restored data points have Std(h_{veg}) < 20 cm). This suggests that the limitation of LiDARs in sensing low vegetation has a low impact on our study. The data restoration step is necessary to avoid considering no vegetation areas where short-statured vegetation exists. Finally, the remaining h_{veg} data are aggregated to the 0.25° grid. Note that 98% of the pixels retain >60% of the original number of 10-m samples after having applied the uncertainty filter and the short vegetation restoring step.
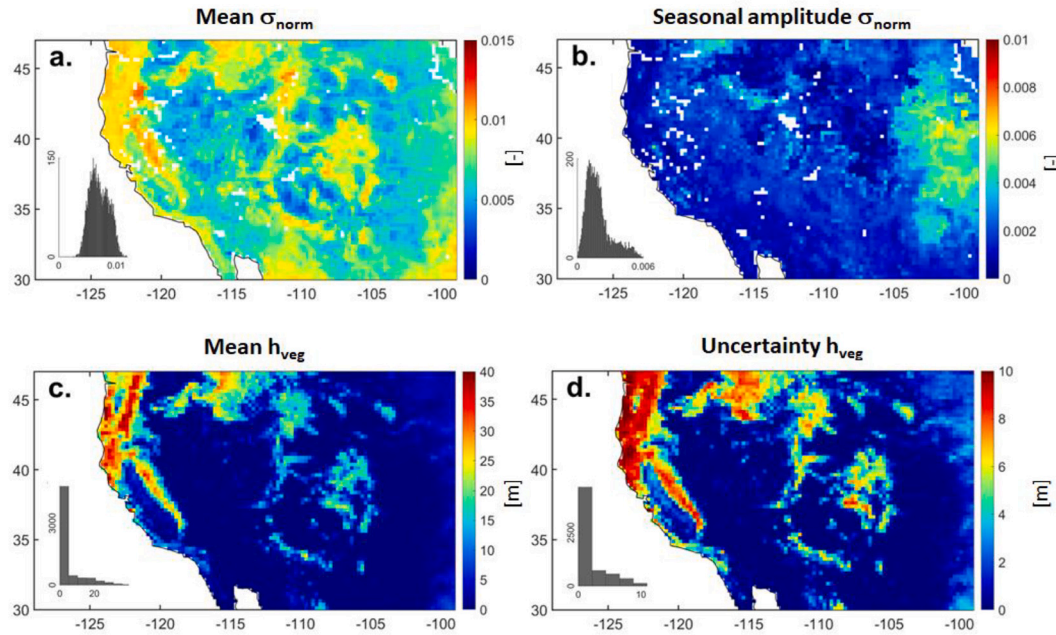
Fig. 2. Mean (a) and seasonal amplitude (b) of the σ_{norm} ([unitless]) for the study period (April 2015 – December 2018) in the western United States. (c) Vegetation canopy height (h_{veg}; [m]) and (d) its uncertainty [m].

The resulting map of h_{veg} is shown in Fig. 2c. The highest canopies (up to 40 m) are in the evergreen forests in the West, while the other forests reach lower canopy heights (~15 m in the Rocky Mountains). In contrast, shrublands dominate most of the region with short canopies (< 1 m). As mentioned before, the short canopies are not sensed accurately by LiDARs, but the inaccuracy is low enough in absolute terms to avoid an impact on the final moisture results. The distribution of h_{veg} per land cover is as expected (Fig. S1e). The uncertainty (in absolute terms) increases with canopy height (Fig. 2d).

2.2.4. In situ LFMC data

In situ LFMC samples from Yebra et al. (2019) have been used for comparison with the retrievals during most of the study period (last *in situ* samples are available in February 2018). Destructive measurements are taken from the top leaves of the canopy and small twigs at approximately 2 pm local time. They are weighted to determine the wet mass, dried at 100 °C, and reweighted to measure the dry mass. LFMC is computed using this information. The samples are daily averaged in case more than one value is available for the same day. In the few cases where one 0.25° pixel includes several sites, data from all sites are averaged.

Importantly, we note that the *in situ* LFMC data is only an approximation of a ground truth for L-band VOD because (i) the sensing depth of SMAP comprises almost the entire canopy, in contrast to the top of the canopy layer from which *in situ* data is sampled; and (ii) at the time of the SMAP overpasses (~6 am local time) vegetation moisture can be different from that at 2 pm, when most plant samples are taken. This is less concerning for AMSR2 VOD (X- and Ku-bands), which senses the top of the canopy at 1 pm local time, reducing the differences in time and in sensing *versus* sampling depths. This limitation is further discussed in Section 4.1.

The number of *in situ* – satellite estimate pairs available for comparison varies depending on frequencies, seasons, and years (Table 1). This is due to the discontinuity of LFMC estimates in 2015 and 2016, the time span of *in situ* and satellite products, and gaps due to snow and frozen ground in winter. The number of *in situ* samples matching with satellite data is 4373 at L-band, 4185 at X-band, and 3804 at Ku-band (Table 1). The distribution of samples in time varies between sites, with one sample every two weeks being the most common configuration. Fig. 3 shows the spatial distribution of the *in situ* sites and the number of sites for each main land cover type.

A main challenge in the comparison of satellite to *in situ* data is the mismatch in spatial scale. Here, the LFMC estimates are produced at a 0.25° grid, and compared with *in situ* data from plants in areas covering only a few meters (Forkel et al., 2022; Rao et al., 2020). For this reason, scaling to the entire pixel can be challenging, particularly in ecosystems with multiple species across multiple edaphic conditions (Konings et al., 2021). To enhance the representativeness of the *in situ* data at the satellite scale, three criteria are used: (i) homogeneity of land cover: sites where the dominant land cover spans through ≥60% of the pixel area are chosen; (ii) homogeneity of species: sites where all the species sampled are of the same vegetation type as the land cover are selected (*e. g.*, sites where all *in situ* data come from shrubland species in pixels dominated by shrublands); and (iii) homogeneity of vegetation surrounding the site: the maximum spatial coefficient of variation of NDVI in the study site ($CV_{NDVI,Max}$) is <0.25. The $CV_{NDVI,Max}$ is provided by Yebra et al. (2019) and applied in previous research (Forkel et al., 2022) using a threshold of <0.26 in that case. It allows screening out sites where the surrounding vegetation is heterogeneous. In addition, a fourth criterion is added concerning sample availability: (iv) Only sites where the number of samples during the study period is ≥10 are selected. Sites fitting all these four criteria are labeled as "homogeneous sites". Sites that do not fulfill these criteria are labeled as "non-homogeneous sites" and are used as complementary information.

Note that, in grasslands, pixels with ≥60% of grassland land cover only match with *in situ* samples taken from shrub species (*i.e.*, criterion (ii) above cannot be fulfilled). Therefore, the homogeneous sites in grasslands must be studied with caution and separately from forests and shrublands by considering this limitation.

Finally, the number of homogeneous sites is 35 (20 in shrublands, 4 in forests and 11 in grasslands), which contain 619, 609, and 526 pairs at L-, X-, and Ku-bands, respectively (Table 1). The homogeneous forest sites are in evergreen needleleaf forests.

2.3. Estimation of vegetation moisture

A multi-sensor VOD estimation algorithm is applied to retrieve the gravimetric vegetation moisture (m_g). It is visually summarized in Fig. 4 and builds on three steps. Step ① models the VOD, step ② minimizes the difference between the modeled VOD and the satellite VOD in order to

Table 1

Number of comparisons between *in situ* and estimates of LFMC by season and year, for all pixels, and for *(homogeneous pixels)*.

Frequency band	TOTAL	Season				Year			
		DJF	MAM	JJA	SON	2015	2016	2017	2018
L	4373	325	1213	1958	877	1319	1630	1401	23
	(619)	*(31)*	*(182)*	*(295)*	*(111)*	*(75)*	*(229)*	*(313)*	*(2)*
X	4185	316	1156	1873	840	1273	1572	1318	22
	(609)	*(31)*	*(177)*	*(291)*	*(110)*	*(74)*	*(227)*	*(306)*	*(2)*
Ku	3804	275	1160	1750	619	1297	1581	926	0
	(526)	*(26)*	*(181)*	*(255)*	*(64)*	*(78)*	*(228)*	*(223)*	*(0)*

DJF: December–January-February; MAM: March–April-May; JJA: June–July-August; SON: September–October-November.
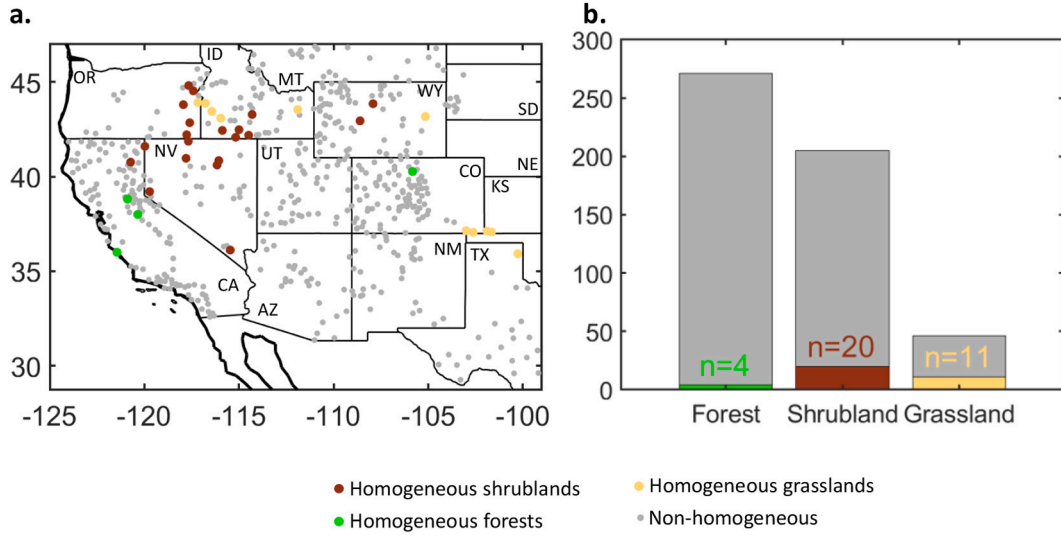
Fig. 3. (a) Location of the *in situ* sites; (b) Number of sites by land cover. *In situ* sites in non-homogeneous pixels are in grey, while those in homogeneous shrublands, forests, and grasslands, are in colour.
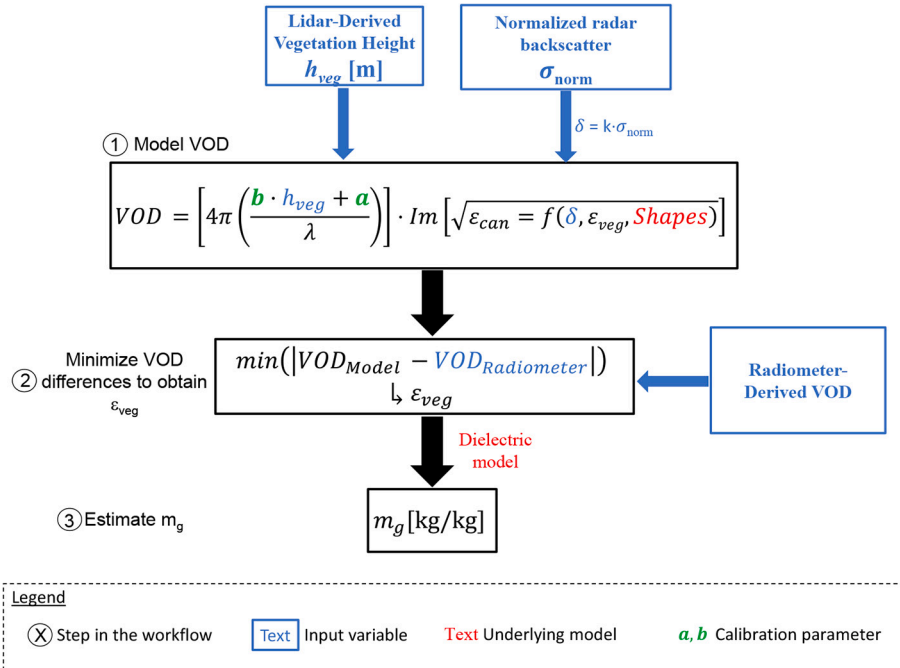
Fig. 4. Workflow of the proposed retrieval approach. In step ① VOD is modeled. In step ② the ε_{veg} value minimizing the differences between the VOD model and the radiometer-derived VOD is found. In step ③ m_g is derived from ε_{veg}.

find the dielectric constant of vegetation (ε_{veg}), and step ③ retrieves m_g from ε_{veg} by using a dielectric mixing model (Fig. 4).

Step ① is based on Eq. (2), which is adapted from Schmugge and Jackson (1992):

$$VOD = 4\pi \left(\frac{b \cdot h_{veg} + a}{\lambda} \right) \cdot Im\left(\sqrt{\varepsilon_{can}} \right), \tag{2}$$

where λ is the wavelength of the passive microwave sensor, h_{veg} is the canopy height, a and b are the calibration parameters, and $Im\left(\sqrt{\varepsilon_{can}} \right)$ is the imaginary part of the square root of the dielectric constant of the canopy.

The basis of the calibration of a and b is formed by building linear regressions of mean VOD as a function of h_{veg} individually for four different bins of σ_{norm} (*i.e.*, different vegetation density levels). By doing so, these regressions represent the relationship between the biomass/structure component and the microwaves attenuation. With h_{veg} and σ_{norm} as controlling parameters accounting for biomass/structure, the main factor leading to VOD variations should be m_g. We assume that the points in the VOD-h_{veg} spaces that match with the regression lines correspond to those with average vegetation moisture ($m_g = 0.5$ kg·kg^{-1}; Table S1 justifies the assumption of this value as an average). Then, points with higher VOD are wetter ($m_g > 0.5$ kg·kg^{-1}) and points with lower VOD are drier ($m_g < 0.5$ kg·kg^{-1}). More details on the calibration approach and justification of the assumptions are provided in Fig. S2 and Appendix A. Table S2 shows the coefficients a and b for each bin and VOD frequency.

The square root of the imaginary part of ε_{can} is applied because it is directly related to the refractive index of the canopy (Cloude, 2010). Since the imaginary part is taken, this approach considers the signal loss of the electromagnetic wave when propagating through a canopy of height h_{veg} (Eq. (2)). Following Ulaby et al. (2014), the ε_{can} is defined as:

$$\varepsilon_{can} = \varepsilon_{host} + \frac{\delta}{3} \left(\varepsilon_{veg} - \varepsilon_{host} \right) \cdot \sum_{u=a,b,c} \left(\frac{1}{1 + A_u \cdot \left(\frac{\varepsilon_{veg}}{\varepsilon_{host}} - 1 \right)} \right), \tag{3}$$

where $\varepsilon_{host} = 1$ (air as host medium), A_u is the depolarization factor which describes the influence of the shapes of the vegetation inclusions on ε_{can}, δ is the radar-derived vegetation volume fraction (δ; [m^3·m^{-3}]), and ε_{veg} is the dielectric constant of the vegetation.

The depolarization factors ($A_u = A_a$, A_b, and A_c) lead to different assumptions of leaf shapes (*i.e.*, shapes of inclusions; De Loor, 1968). Here, the random needles assumption is chosen ($A_a = A_b = 0.5; A_c = 0$) as justified in Appendix B. The vegetation volume fraction (δ) is the volume proportion of solid vegetation material, as sensed by a microwave sensor, in a voxel of air. It accounts for vegetation structure and dry biomass. The parameter δ is directly proportional to σ_{norm} (Fink et al., 2018; Chaparro et al., 2021):

$$\delta = k \cdot \sigma_{norm}, \tag{4}$$

where k is a constant value. Here, the value of k has been set to 0.05 leading δ to range from $4 \cdot 10^{-3}$ to 0.01, which is consistent with literature (Choudhury et al., 1994; Schmugge and Jackson, 1992; Ulaby et al., 1983; Wigneron et al., 1993). According to our sensitivity analyses, the application of different k values does not lead to relevant differences in the m_g outputs (not shown). This is because k (in Eq. (4)) and b (in Eq. (2)) are constants in the algorithm compensating each other. In this study, we account for the time dynamics of δ when estimating m_g but also explore complementarily the impact of using a time-static δ. It is computed from the time average of σ_{norm} at a pixel basis and used to compare the results with the dynamic approach.

In step ②, the dielectric constant of vegetation (ε_{veg}; unknown) is obtained by an optimization procedure minimizing the difference between the modeled and the observed VOD from SMAP (L-band) or AMSR2 (X- and Ku-bands). Finally, in step ③, m_g is estimated from ε_{veg} using another dielectric mixing model. Here, the model proposed by Ulaby and El-Rayes (1987) has been applied:

$$\varepsilon_{veg} = \varepsilon_r + v_{fw} \cdot \varepsilon_{fw} + v_{bw} \cdot \varepsilon_{bw}. \tag{5}$$

This model assumes that ε_{veg} is a mixture of three components: a non-dispersive residual component (ε_r), a free-water component ($v_{fw} \cdot \varepsilon_{fw}$), and a bulk vegetation-bound water component ($v_{bw} \cdot \varepsilon_{bw}$). Importantly, each one of these three components are a function of m_g, temperature, salinity, and frequency. The m_g can be retrieved because temperature and salinity are fixed to 22 °C and 8.53‰ (in agreement with Ulaby and El-Rayes, 1987), and the frequency is known.

To test the consistency of the results, two other dielectric mixing models for m_g estimation have been explored: the empirical models from Li et al. (2014) and Matzler (1994). The latter was designed only for $m_g > 0.5$ kg·kg^{-1} so here a linear extrapolation is used for lower values. Fig. S3 shows the m_g - ε_{veg} relationship for each dielectric mixing model and frequency.

2.4. Conversion from m_g to LFMC and comparison with in situ data

The estimates of m_g are converted to LFMC units for comparability with the *in situ* data:

$$LFMC = \left(\frac{m_g}{1 - m_g} \right) \cdot 100. \tag{6}$$

LFMC is usually expressed as a percentage of the mass of vegetation water per unit of dry biomass and may range between ~25% ($m_g = 0.2$ kg·kg^{-1}) and 400% ($m_g = 0.8$ kg·kg^{-1}) in living plants. When the water and dry biomass amounts are equivalent, then LFMC = 100%, and $m_g = 0.5$ kg·kg^{-1} (the average moisture value). Values of LFMC below 25% are normally found in dead vegetation. Concerning high LFMC values, the 99th percentile of the Globe-LFMC database in Yebra et al. (2019) is 255% ($m_g = 0.72$ kg/kg).

The comparison analyses are performed in three steps. First, the overall consistency of the retrievals is studied by computing the differences between *in situ* and remotely-sensed LFMC, and by comparing the monthly distribution of the results and the *in situ* samples. Second, the Pearson's correlation coefficient (r), the root mean square error (RMSE) and the bias are computed for all *in situ*-estimate pairs for different land covers, δ configurations (static or dynamic), and dielectric mixing models of vegetation. Third, analysis of each station separately is performed by (i) analyzing the impact of the *in situ* variability on r (see Rao et al., 2020), (ii) computing r, RMSE and bias for each homogeneous site, and (iii) showing examples of time series of LFMC retrievals compared to *in situ* LFMC data.

3. Results

3.1. Satellite-derived LFMC maps and overall consistency of the retrievals

Fig. 5 presents the time-averaged maps of LFMC [%] estimates during the study period (April 2015–December 2018) and the bias for each *in situ* site. L-band LFMC (hereafter L-LFMC) reveals a different spatial distribution and more variability (Fig. 5a) than X- and Ku-band LFMC (hereafter X- and Ku-LFMC; Fig. 5c and e). A dry to wet transition from South to North is observed at X- and Ku-bands, with most biases ranging between 40% and +40% (Fig. 5c-f). Note that such biases correspond to approximately ±10% of the dynamic range of LFMC, which varies between 25% and 400%.

L-LFMC retrievals show wet regions with overestimations in the central-South area and in the Southwestern coast. These areas show drier conditions with X- and Ku-LFMC, with biases close to 0% at these frequencies in the South-West (Fig. 5). In the North-central and North-East regions, X- and Ku-LFMC show wet vegetation in contrast with
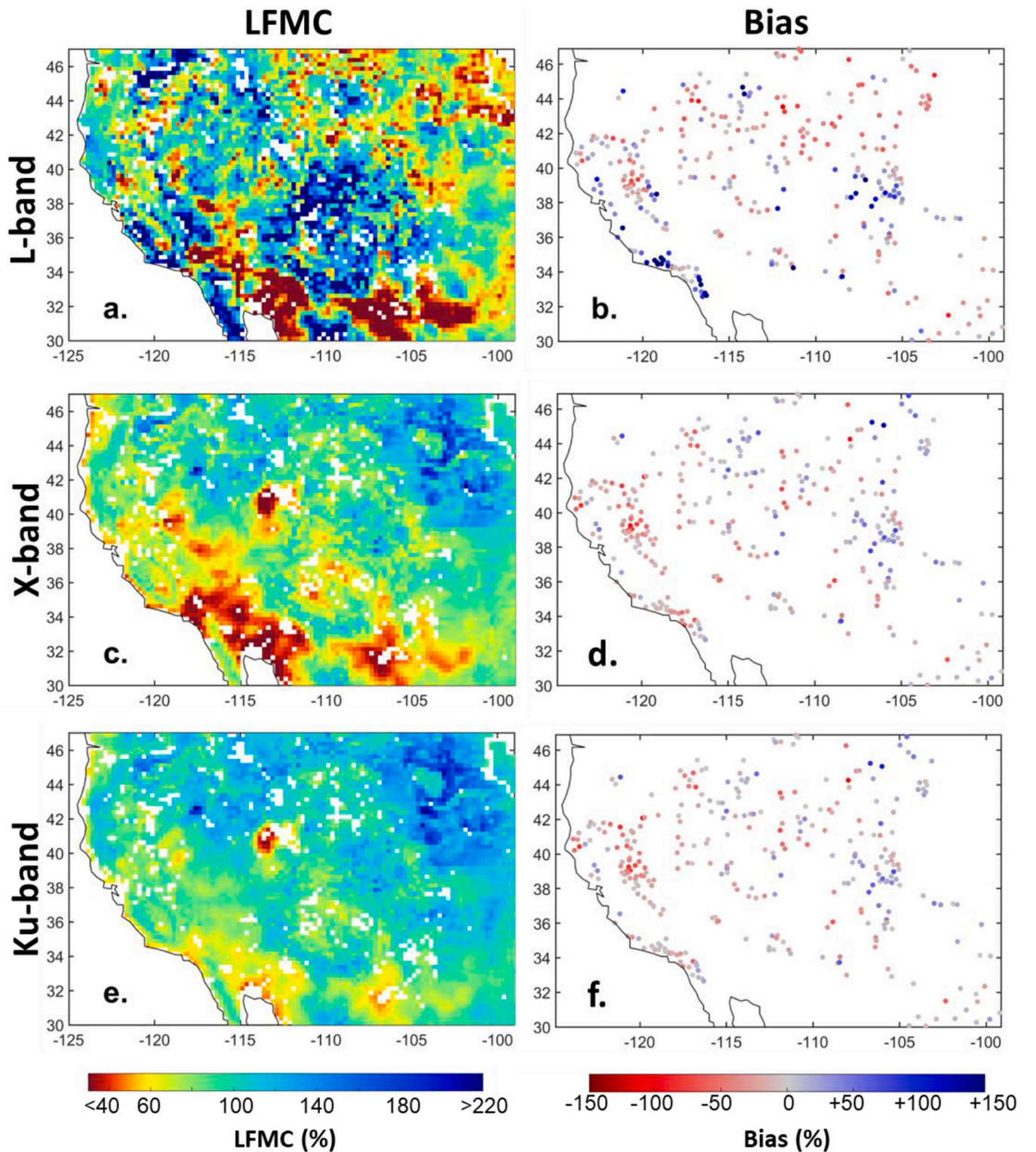
Fig. 5. Left column: maps of mean LFMC in time along the study period (April 2015 – December 2018). Right column: maps of bias for estimates minus *in situ* comparisons at each individual site (both homogeneous and non-homogeneous sites included). Frequency bands are L-band (a-b); X-band (c-d); and Ku-band (e-f).

dry patterns at L-band. The latter shows larger biases in absolute values. Finally, retrievals in forests in the western mountain ranges are consistent among frequencies, where LFMC is underestimated (Fig. 5).

Fig. 6 shows the distribution of the satellite-based LFMC estimates (0.25° pixel) and of their corresponding *in situ* sites (point-based) for the entire study region and all dates. The mode and median of the retrievals match those of the *in situ* dataset. The spread of LFMC estimates is larger

at L-band and narrower at X- and Ku-bands (Fig. 6a-c). Fig. 6(d-f) shows histograms of differences between *in situ* and estimates. L-LFMC has important overestimation (up to +150%), and only 48% of the estimates are in a reasonable range (−40% to +40%; Fig. 6d). This percentage is much larger for X- (76%) and Ku-LFMC (77%; Fig. 6e-f).

Considering time dynamics, Fig. 7 shows the median and standard deviation of estimates and *in situ* data for each month (all years
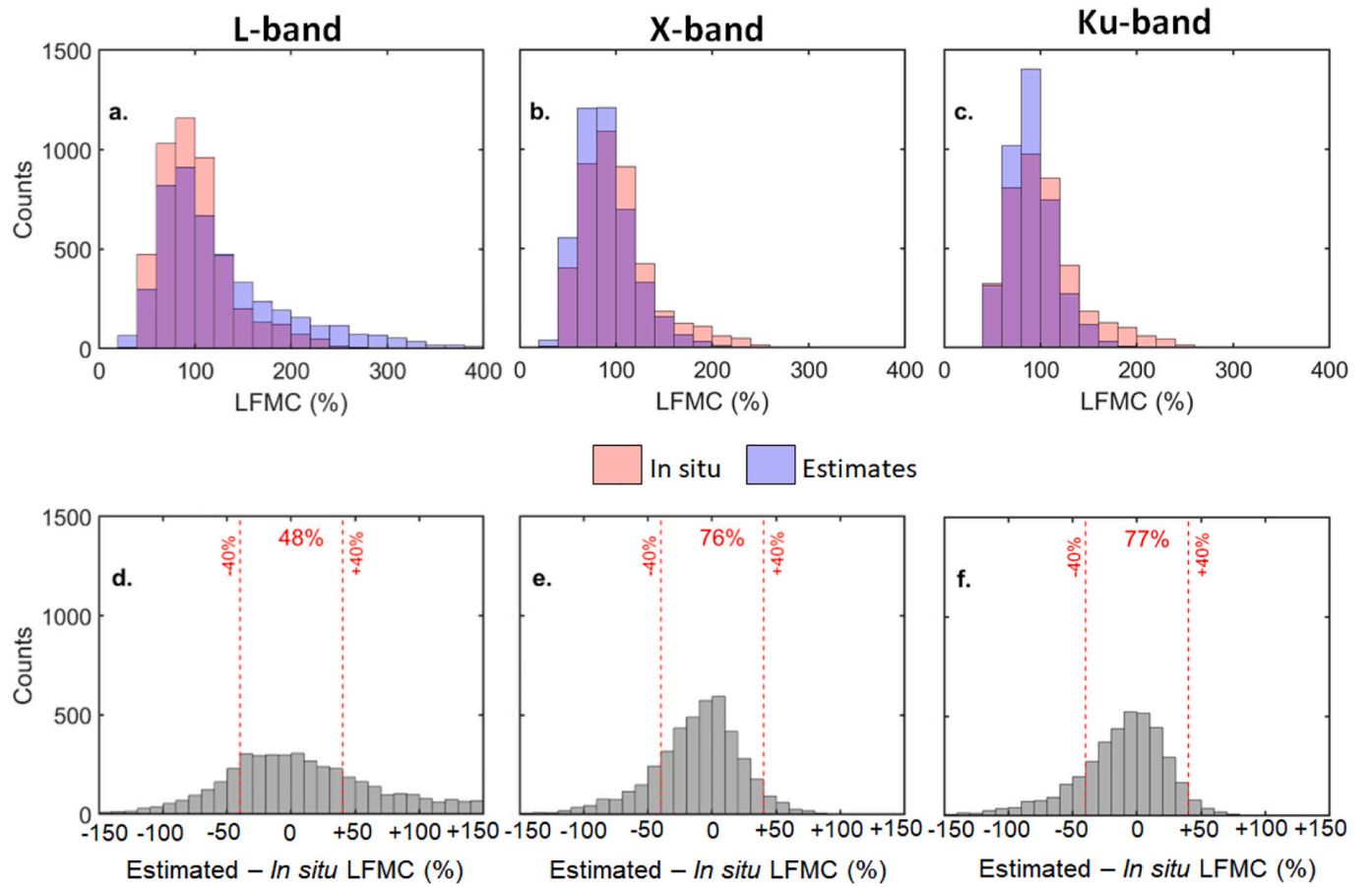
Fig. 6. Top row: comparison between *in situ* (pink) and estimated (blue) LFMC for (a) L-band, (b) X-band and (c) Ku-band. Bottom row: histogram of the differences between estimated and *in situ* LFMC for all samples available at (d) L-band, (e) X-band and (f) Ku-band. Dashed red lines indicate deviations of ±40% in LFMC units, which corresponds to approximately ±10% in the dynamic range of the variable. (For interpretation of the references to colour in this figure legend, the reader is referred to the web version of this article.)
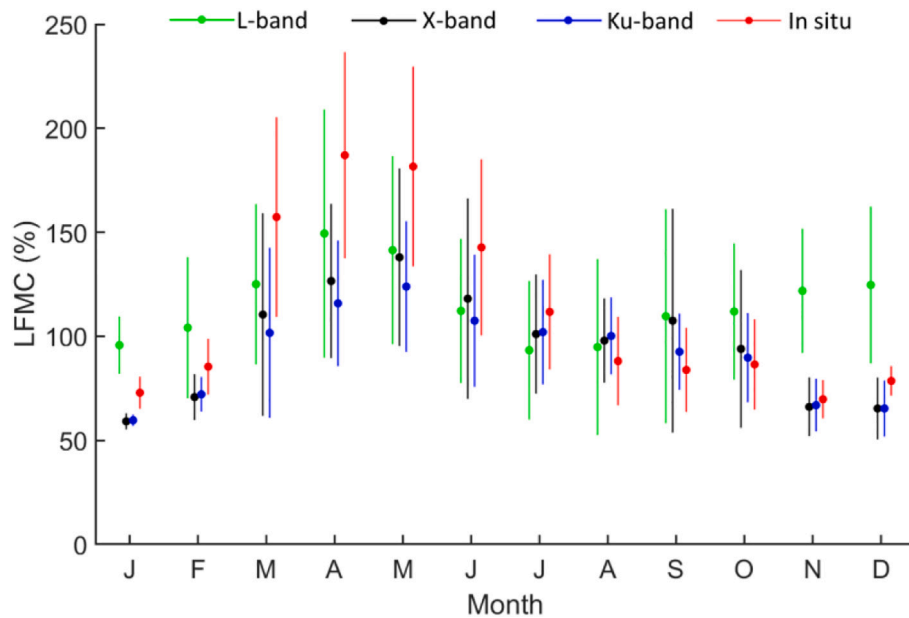
Fig. 7. Comparison of spatially and monthly averaged *in situ* (red) and estimated (green: L-band; black: X-band; blue: Ku-band) LFMC computed along the entire study period. Each point shows a monthly median, and bars correspond to ±1 standard deviation of LFMC. Here, only *in situ* – estimate pairs for homogeneous sites have been used. (For interpretation of the references to colour in this figure legend, the reader is referred to the web version of this article.)

included). All frequencies capture an increase in the LFMC from January to April, and a decrease from May to August, consistent with the *in situ* samples and with the precipitation patterns in this area. In September and October, *in situ* samples show roughly constant values. They decrease in November and December because all, except southern (dry) sites, are screened out due to snow and frozen ground conditions. Both X- and Ku-LFMC track well the behavior of the *in situ* measurements between September and December, while L-LFMC shows a distinct increase towards higher values. We hypothesize that the hydric status in woody parts of the plants, sensed by L-band, could remain high with increasing precipitation during this season even in dry areas, but further analysis would be required using *in situ* samples from deeper vegetation layers to verify this. These samples are unfortunately unavailable.

Fig. 8 shows that results are independent of σ_{norm} and h_{veg}. Given that the density and height of vegetation are proxies of biomass, this indicates that the algorithm removes at least a relevant part of the biomass effect on the VOD signal, mostly keeping the water component of it.

3.2. Results for different land covers, dielectric models, and δ configurations

Fig. 9 shows scatterplots of the comparison between LFMC satellite estimates and *in situ* measurements for all times and dates. In homogeneous pixels and regardless of the land cover, X- and Ku-LFMC show a good Pearson's correlation ($r = 0.60$ and $r = 0.64$, respectively), which is lower at L-band ($r = 0.37$). In non-homogeneous pixels, only X- and Ku-bands show positive correlations (r ~ 0.4; Fig. 9a-c). The error (RMSE) is expressed in LFMC units [%] and decreases with increasing frequency: 44% at L-band, 33% at X-band, and 22% at Ku-band. The bias ranges between −11% and − 25%.

In shrublands, the correlations are moderate and similar between frequencies in homogeneous pixels ($r = 0.46$ at L-band, $r = 0.51$ at X-band, and $r = 0.54$ at Ku-band), while in non-homogeneous pixels they are non-significant at L-band, and lower at X- and Ku-bands (0.47 and 0.41, respectively). In forests, the correlation is negative at L-band (*i.e.*, without physical sense). At X- and Ku-bands, correlations are good (r ~ 0.6) and slightly higher in forests if a static, time-averaged δ is applied instead of a variable one (Fig. 9g-l and Table S3). Fig. 10 shows the results for grasslands. Despite of the limitation in grassland *in situ* sampling, correlation is found for X-LFMC ($r = 0.44$) and Ku-LFMC ($r = 0.33$), although the slopes of the regressions indicate that the sensitivity

is lower than for shrubs and forests.

We also calculated the correlations of the *in situ* LFMC directly with the satellite-derived VOD (see Fig. S4). For homogeneous pixels in shrublands and forests, the correlation is higher for LFMC estimates (0.37, 0.60, and 0.64 for L-, X- and Ku-bands, respectively) than for VOD (non-significant, 0.39 and 0.43). Finally, note that the use of different dielectric models does not change the results significantly (Table S3).

3.3. Comparison between in situ samples and satellite estimates at a pixel-site basis

Fig. 11(a-c) shows the comparison between the standard deviation in time of *in situ* LFMC and that of the estimated LFMC for shrub and forest sites. The regression slope is closer to the 1:1 line at L-band and decreases with frequency. However, this comes with the cost of a higher spread of points, with larger RMSE and lower correlation, especially at L-band, as compared to X- and Ku-bands.

Following Rao et al. (2020), we also analyzed the correlation between the *in situ* variability and the Pearson's correlation between *in situ* and estimates. Fig. 11(d-f) shows a positive correlation, between 0.54 and 0.77 depending on the frequency. Fig. 11d-f also reports that the percentage of sites with high correlation (r > 0.5) is large at X- and Ku-bands (75%), and lower at L-band (54%). Importantly, most sites with low correlation show a low standard deviation of *in situ* samples (Fig. 11) as the correlation between flat time series is dominated by noise and does not offer a good comparability (Rao et al., 2020).

Fig. 12 provides six examples of time-series of X-LFMC retrievals on specific pixels and their corresponding *in situ* (see Figs. S5 and S6 for L- and Ku-bands, respectively). The sites plotted are those showing the highest *in situ* variability to maximize the comparability. These sites are dominated by shrublands with different canopy densities (*e.g.*, compare images in Fig. 12b and e). In general, all time-series show drying trends in summer and, when data is available, wetting trends in fall 2016 and spring 2017. These patterns are consistent with the *in situ* ones and with Fig. 7. Correlations are high or very high, ranging between 0.64 (Fig. 12a) and 0.94 (Fig. 12e). The regression slope in the latter case is very close to the 1:1 line, being the best-performing example. RMSE is between very low (6% in LFMC units) and moderate (36%), and bias shows good agreement in most cases (≤30%) except for the underestimation in Fig. 12d (bias = −67%) which is the case with the worst (almost zero) sensitivity. In all cases, the continuity of the time series is hampered by winter and by the sparsity of
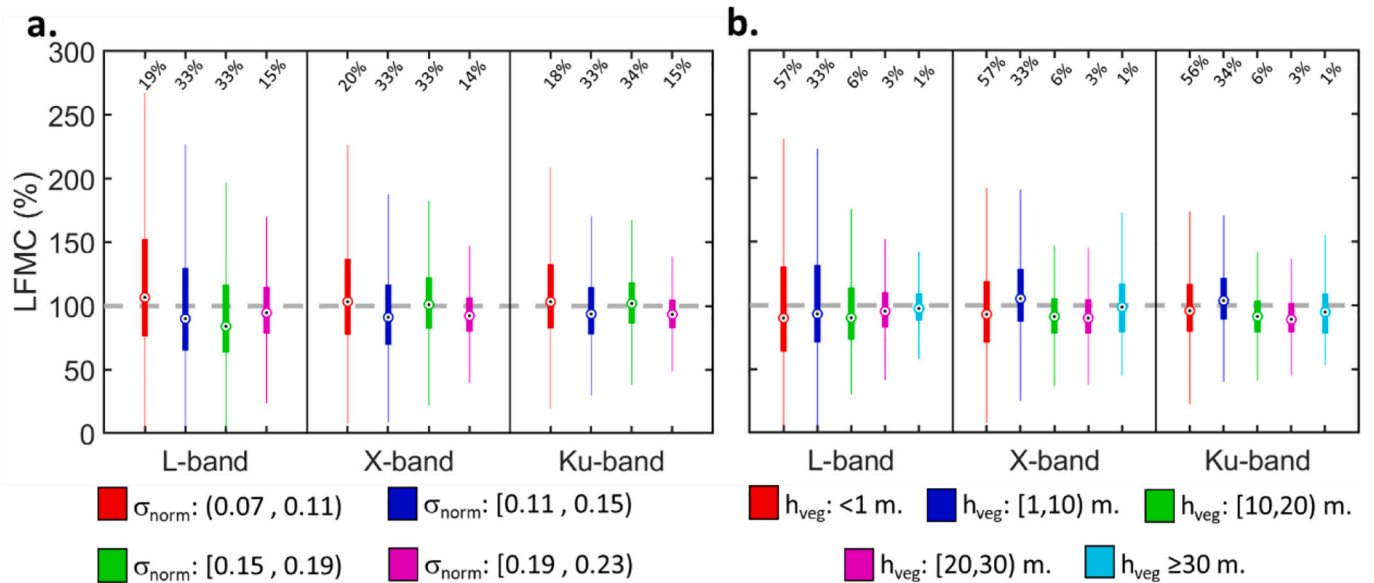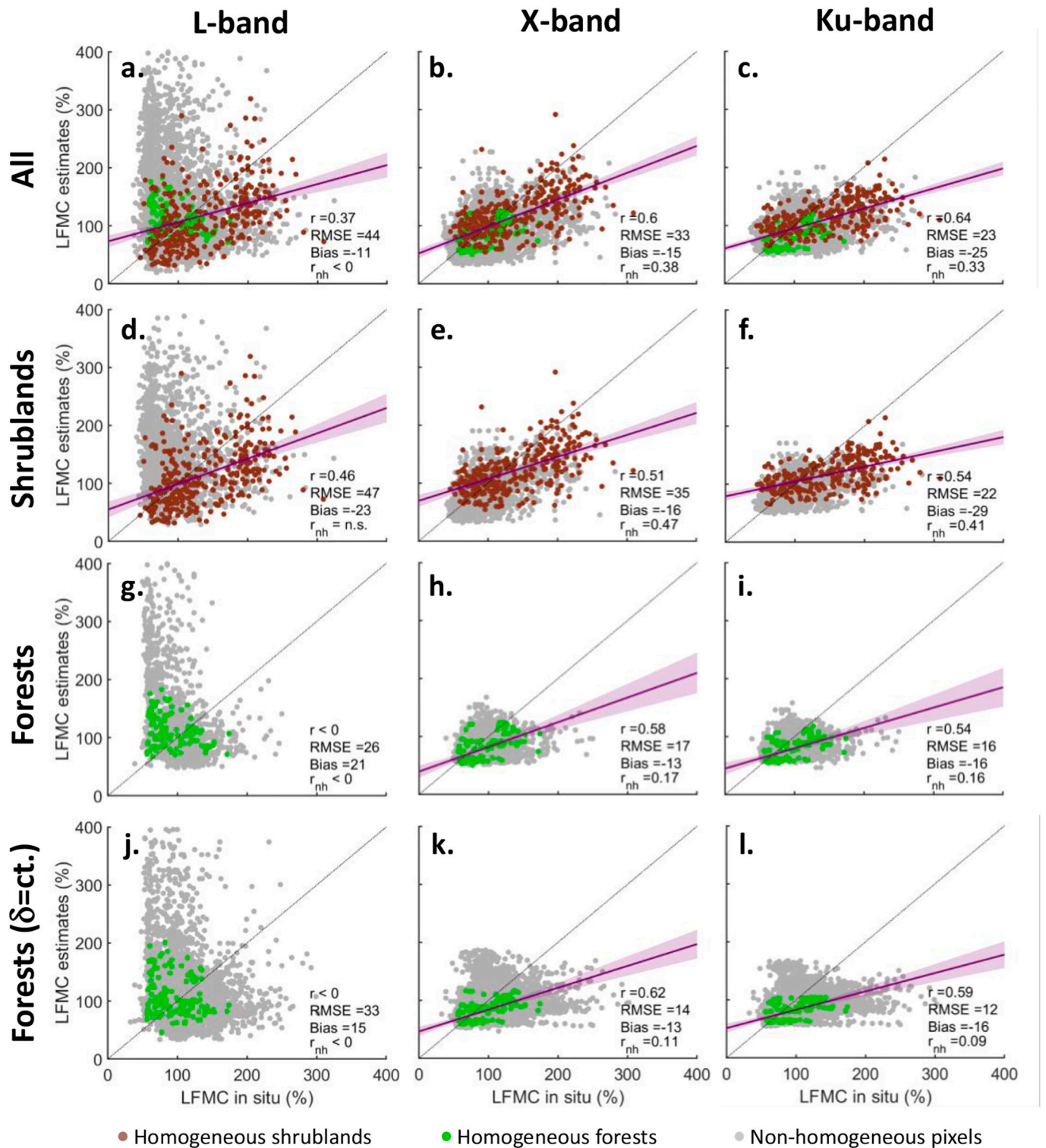

Fig. 8. Results of LFMC estimates for each frequency, classified by (a) σ_{norm} bins (those used in the calibration) and (b) h_{veg} bins. Percentages indicate the relative number of samples per bin. The grey line is used as a reference of the LFMC = 100% (m_g = 0.5 kg·kg^{-1}) value.
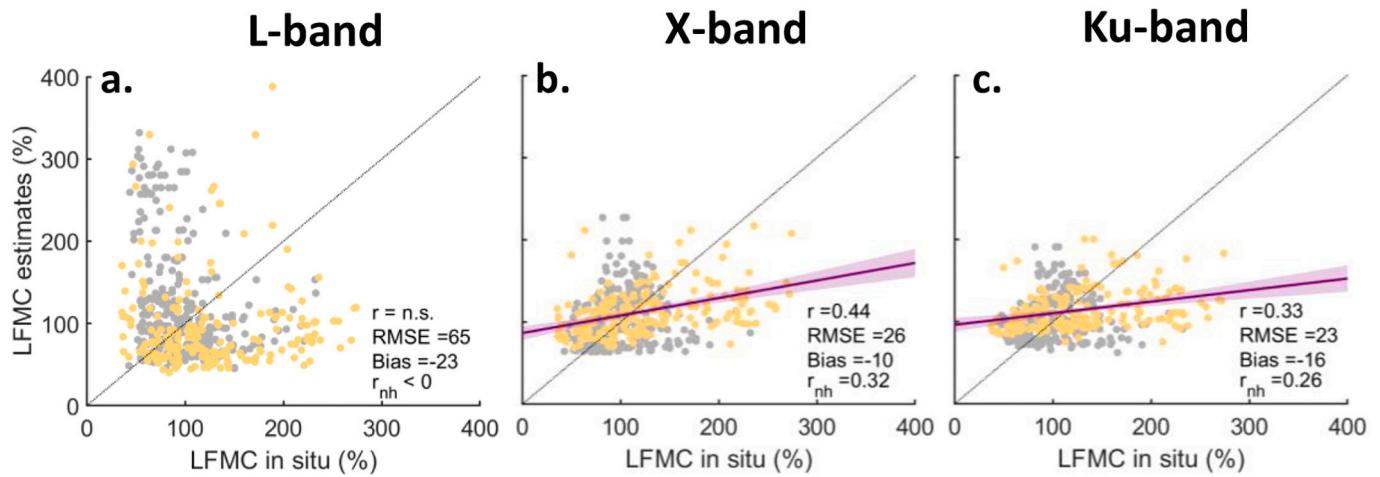
Fig. 9. Comparison between *in situ* LFMC and satellite-derived LFMC estimates for shrub and forest sites and all dates. The estimates are based on the dielectric model from Ulaby and El-Rayes (1987). The homogeneous pixels are in brown (shrublands) and green (forests), and the non-homogeneous in grey. Statistics are computed for homogeneous pixels: r, RMSE [%] and Bias [%]. Percentages are in LFMC units. Correlation for non-homogeneous pixels is also added for comparison (r_{nh}). Left column: L-band; central column: X-band; right column: Ku-band. First row (a-c): both land covers; second row (d-f): shrublands; third row (g-i): forests; and fourth row (j-l): forests using a static, time-averaged δ. (For interpretation of the references to colour in this figure legend, the reader is referred to the web version of this article.)

Sentinel-1 data in 2016 (see Section 2.2.2). Also, some jumps are detected in the time series, especially in Fig. 12b (May, July, and October 2017) and in Fig. 12d (May 2017). They can be explained by rapid changes in VOD contrasting with smoother variations in the δ component.

Statistics for shrub and forest sites are in Table S4. In most cases, results at X- and Ku-bands outperform those of L-band which, still, shows good correlation ($r > 0.5$) and low error and bias ($<40\%$) in approximately 50% of sites over shrublands. At X- and Ku-bands, correlations are high ($r > 0.5$)

Fig. 10. Comparison between *in situ* LFMC measurements and LFMC estimates for sites in grassland land cover pixels and for all dates. The homogeneous pixels are in yellow and the non-homogeneous in grey. The LFMC estimates are based on the dielectric model from Ulaby and El-Rayes (1987). (a) L-band; (b) X-band; and (c) Ku-band. Note that grasslands are not shown together with other land covers in Fig. 9 due to limitations of *in situ* data in this land cover type (see Section 2.2.4). (For interpretation of the references to colour in this figure legend, the reader is referred to the web version of this article.)
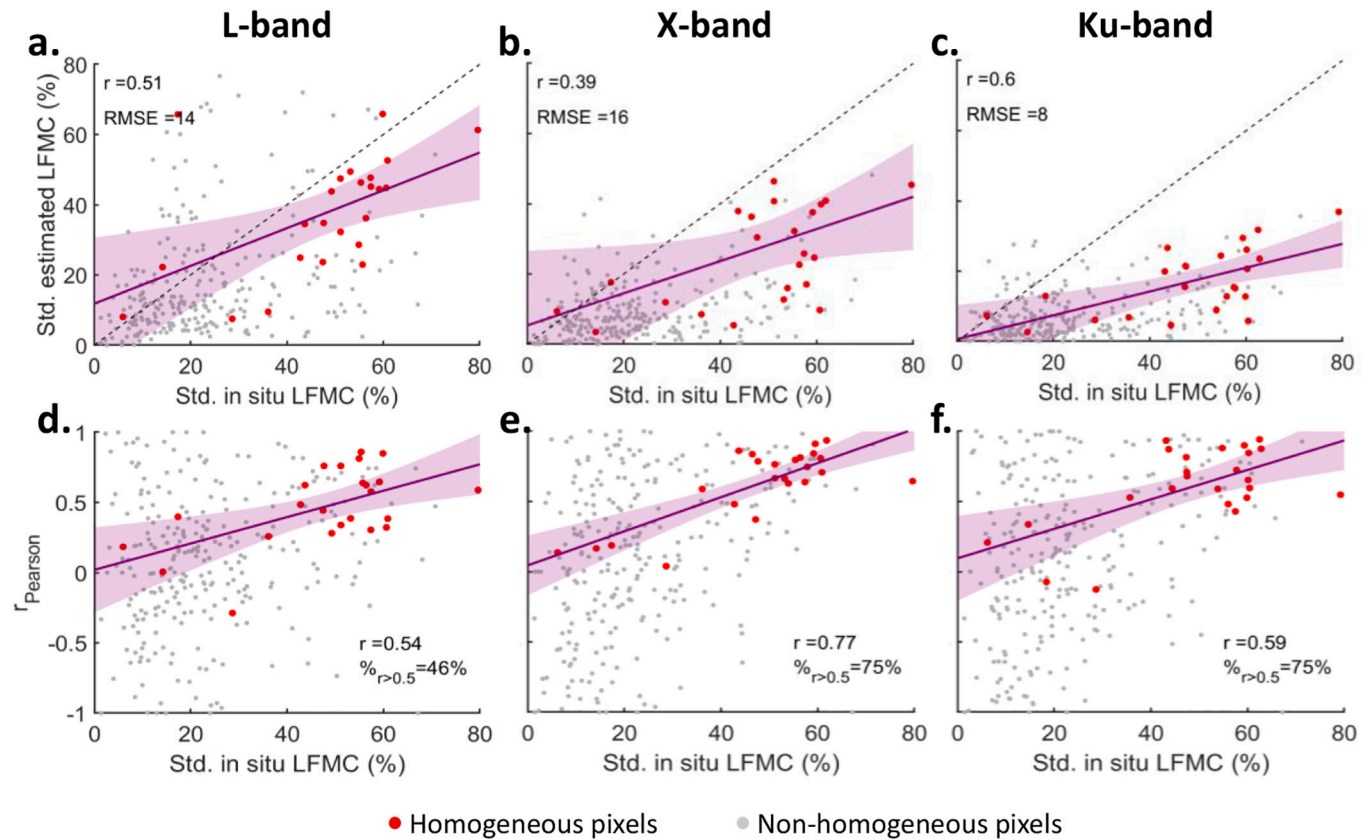
Fig. 11. (a-c) Relationship between the standard deviation of *in situ* and estimated LFMC time series for L-, X- and Ku-bands, respectively. (d-f) Relationship between the standard deviation of *in situ* LFMC time series and the Pearson's correlation coefficient between *in situ* values and estimates, for L-, X- and Ku-bands, respectively. Red: homogeneous pixels. Grey: non-homogeneous pixels. Regression lines and Pearson's correlation coefficients are based on the homogeneous cases. The value "%$_{r>0.5}$" refers to the percentage of homogeneous sites where correlation is higher than 0.5. The analysis is conducted in forest and shrub sites.

in ≥75% of cases and even very high ($r > 0.8$) in some sites (Table S4). RMSE is low (<40%) in all except one site at X- and Ku-bands (*Balanced Rock*), and bias is between −40% and +40% in most cases. In forests, the site with the highest *in situ* LFMC standard deviation (36%) shows a good correlation ($r > 0.5$), while the remaining three sites have very low *in situ* variability and non-significant and low correlations. At the four forest sites, however, RMSE and bias show low errors (Table S4).

Table S5 shows the results for grasslands, where correlations are mostly non-significant at L-band, with higher RMSE and bias than at X- and Ku-bands. At these higher frequencies, most sites show positive correlations (between 0.48 and 0.93) and low RMSE and bias values (<30%). Underestimations are found in three sites: *Keeney, Idaho Falls*, and *Wild West* (bias < −60%; Table S5).
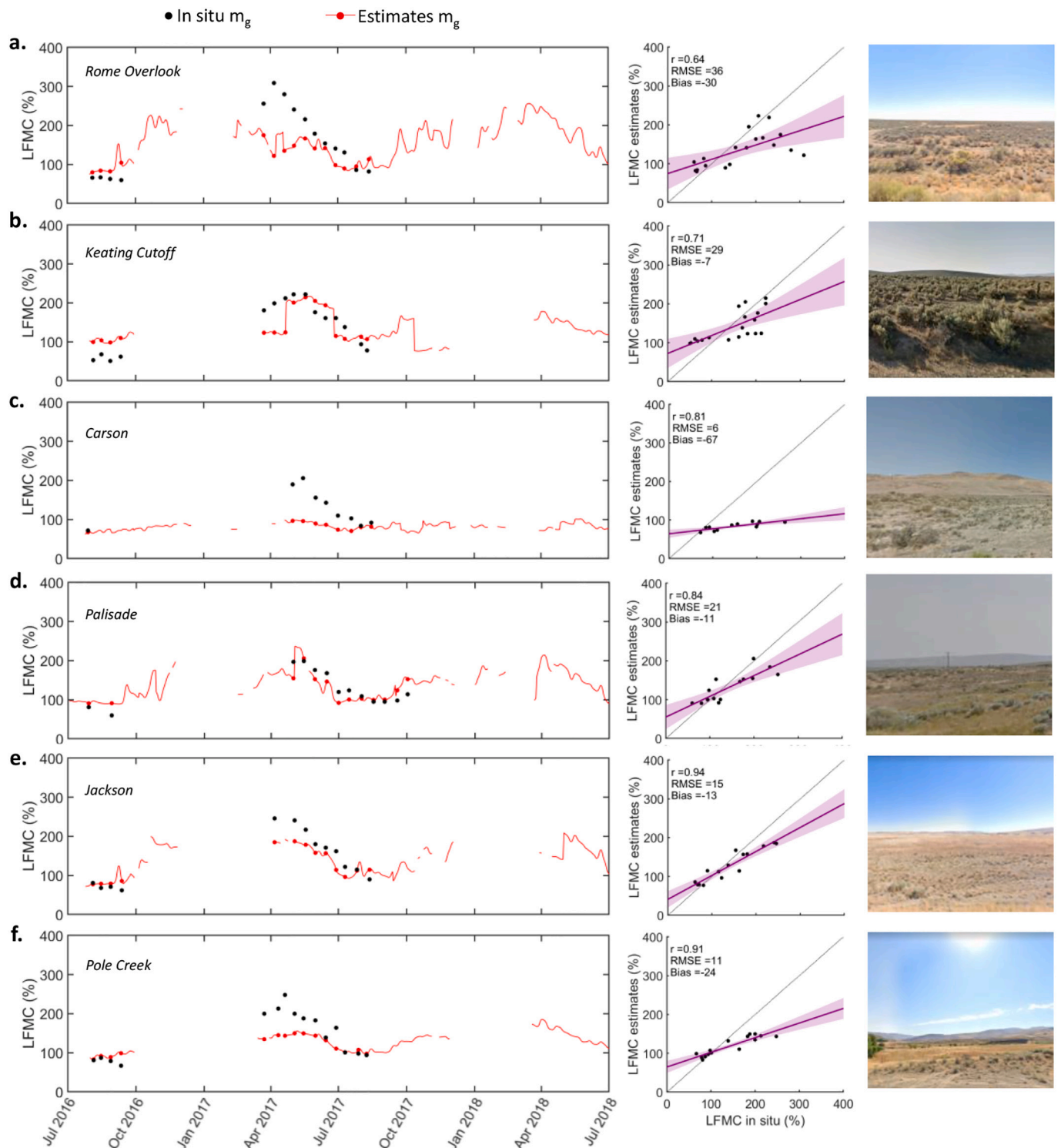
Fig. 12. Time-series at six sites showing the comparison between X-LFMC and *in situ* LFMC. The selected sites are the six homogeneous sites with larger standard deviation of *in situ* LFMC, to guarantee enough *in situ* variability and pixel homogeneity for providing a fair *in situ vs.* estimate comparison. The site names are: (a) *Rome Overlook*; (b) *Keating Cutoff*; (c) *Carson*; (d) *Palisade*; (e) *Jackson*; and (f) *Pole Creek*. Further details on these stations are in Table S4. Images for each site are from Google Street View™.

4. Discussion

4.1. Extracting vegetation moisture from vegetation optical depth at multiple frequencies

The LFMC retrievals show good agreement with *in situ* measurements

and literature values in terms of data distribution and median, with slight underestimation, at X- and Ku-bands (Fig. 6 and Table S1). The maps of average X- and Ku-LFMC qualitatively match the expected spatial patterns, with a dry to wet transition from South to North in the Western United States. The dry vegetation in the South is consistent with the LFMC dataset from Rao et al. (2020).

Importantly, the LFMC satellite estimates are independent of the biomass and structure effects that are imprinted in the VOD signal. This is evaluated with canopy height and the radar-derived index, two variables tightly linked to biomass (Fig. 8; Bouvet et al., 2018; Baccini et al., 2008). The result is confirmed by the lack of land cover effect in the comparison between *in situ* and estimates of LFMC (Fig. 9; shrubs and forests points are merged). This contrasts with clear land cover imprint in the comparison between VOD and *in situ* LFMC, especially at L-band (Fig. S4; shrubs and forests points are clustered). Moreover, the correlation between LFMC retrievals and *in situ* LFMC is higher than the correlation between VOD and *in situ* LFMC, suggesting an enhanced capacity of the proposed retrievals to track water content at the regional scale than with VOD (Figs. 9 and S4).

Compared to *in situ* data, X- and Ku-LFMC show good (r ≈ 0.60) and moderate (r ≈ 0.40) correlations for homogeneous and non-homogeneous pixels, respectively. This is in line with Rao et al. (2020; $r = 0.79$), where the higher correlation can be explained by the much higher spatial resolution used in their study (250 m). Thus, the results are accurate enough to track the time dynamics of *in situ* LFMC despite the large spatial scale mismatch between the measurement sites and the satellite resolution cell. In that sense, our LFMC retrievals reasonably track vegetation moistening and drying according to seasons both in general (Fig. 7) and in site-to-pixel comparisons (Fig. 12). The latter showcases the suitability of the algorithm to retrieve LFMC not only regionally but also at pixel scale, with high correlations in most comparisons (Fig. 12 and Table S4).

At L-band, results show poorer performance (Fig. 6) likely due to three reasons. First, the coarser native resolution of the L-band can explain part of the differences in correlation. Second, the time when most *in situ* samples were taken (around 2 pm) is different from that of the SMAP overpasses (6 am). This limits the interpretability of L-band results because, while in predawn conditions leaf and full canopy moisture should be in equilibrium in low biomass vegetation (*e.g.*, shrublands), such balance can be lost during midday when leaf water losses increase rapidly due to transpiration (*i.e.*, LFMC decreases). This limitation is also applicable for differences between drought and non-drought conditions during the study period. Third, L-VOD is sensitive to water and biomass changes in the deeper canopy layers and the woody components of the canopy (Li et al., 2021; Bueso et al., 2023). In forests, we acknowledge that the comparison of L-LFMC with top of the canopy *in situ* measurements is also limited by vertical gradients in hydraulic traits and water potential and thus, likely, in the moisture content (Couvreur et al., 2018). Because the *in situ* LFMC measurements are taken from the top leaves of the canopy (Yebra et al., 2019), it is expected that frequencies with shallower sensing depth (X- and Ku-bands) reveal better agreement with *in situ* measurements (Forkel et al., 2023; Rao et al., 2020). A similar conclusion has been found for other leaf-related variables (Konings and Gentine, 2017; Schmidt et al., 2023; Teubner et al., 2018). In addition, it has been confirmed that L-VOD is the most appropriate frequency to sense dense vegetation canopies (Chaparro et al., 2019). However, X-VOD has a higher sensitivity to short vegetation such as that dominant in the study area (Olivares-Cabello et al., 2022). We hypothesize that L-LFMC would provide a better agreement when compared to *in situ* samples from woody parts in dense vegetation. In this regard, Holtzman et al. (2021) have shown good agreement between xylem hydric potential and L-VOD using a tower-based L-band radiometer in the Harvard forest (MA, USA).

4.2. Effect of land cover, vegetation homogeneity, and δ variability on the LFMC retrievals

Results vary according to land cover types and the homogeneity of the vegetation within each pixel. In shrublands, LFMC retrievals at all frequencies show moderate correlation ($r > 0.5$) with *in situ* data, although lower error confirms the improved performance of higher frequencies. Interestingly, non-homogeneous pixels also show moderate

agreement ($r > 0.4$) at X- and Ku-bands (Fig. 9). This happens likely because this land cover type is dominating large areas of the study region (Fig. S1a), with most pixels containing large fractions of shrublands even if they do not fulfill the homogeneity criteria.

In grasslands, the lack of *in situ* measurements taken from grass species hampers the assessment of the LFMC estimates. Despite this limitation, a correlation between satellite and *in situ* data is found at X- and Ku-bands both regionally (Fig. 10; $r > 0.3$) and in most sites (Table S5). In grasslands, the large seasonal amplitude of VOD (Fig. 2d and f) and the large annual dynamics of δ (Fig. S1d) suggest that a dynamic vegetation height input should also be considered for this land cover type to enhance the retrievals.

In forests, good agreement at regional scale is found at X- and Ku-bands (Fig. 9). The uncertainty of h_{veg} and VOD data in forests may still largely impact the retrievals (see Section 4.3). Moreover, using only four homogeneous sites limits the comparison between *in situ* data and satellite retrievals. This screening by homogeneity is necessary to deal with the site-to-pixel spatial scale mismatch, as shown by the fact that homogeneous sites yield a much higher correlation (r ≈ 0.6) as compared to non-homogeneous sites (r ≈ 0.2; Fig. 9) for X- and Ku-bands in forests. Another major consideration for forests is the reduced temporal *in situ* variability (Table S4), which strongly hampers the comparability between *in situ* data and our retrievals (Fig. 11 and Rao et al., 2020). Notably, the *Marshall Grade* site is the forest site with the highest *in situ* variability and the one showing good correlations (Table S4).

Concerning L-LFMC, its lack of capacity to track forest moisture can be explained by several factors. First, the fact that vegetation moisture in leaves and twigs (from *in situ* data) can largely differ from that of trunks and branches (sensed by L-band) making the site samples not representative of the fraction of canopy seen by L-band microwaves. Second, the fact that zeroth-order scattering is assumed in the τ-ω model used for VOD retrievals (Mo et al., 1982), while the type of scattering occurring in forests can be of higher orders at L-band (Feldman et al., 2018). Third, Xu et al. (2021) have shown that leaf canopy interception drives variations of VOD in dense forests to a greater extent than hydric stress. Then, the assumption of vegetation moisture being the only factor driving VOD variability for known h_{veg} and σ_{norm} values (Section 2.3) may be compromised in the dense western forests.

The improved correlation obtained with the static δ parameter in forests (Fig. 9) is likely due to the low variability of forest density over time. This can cause that noise rather than phenology dominates in the dynamic δ approach. On the contrary, results for all land covers at X- and Ku-bands indicate that the use of a dynamic radar-based parameter is necessary (Table S3).

4.3. Future satellite missions could overcome limitations and uncertainty in LFMC retrievals

The application of three satellite products as inputs to retrieve LFMC may lead to uncertainties that should be considered. First, h_{veg} data has shown systematic underestimation in high canopies (Lang et al., 2022), where the h_{veg} uncertainty is large (Fig. 2b). However, the comparison between *in situ* and estimates in forests has not shown large differences in sensitivity, correlation, bias, and error as compared to shrublands, in the case of homogeneous pixels (Fig. 9). This suggests that the impact of h_{veg} uncertainty in forests is limited. Concerning short vegetation (<5 m.), the h_{veg} product has shown some overestimation (Lang et al., 2022) and high relative uncertainty (even >50%; Fig. 2), but this uncertainty is low in absolute terms and has a low impact in the results. Despite these limitations, the applied product is the only global satellite-derived canopy height dataset reporting h_{veg} information for all land cover types, while previous products are only focused on forests (Potapov et al., 2021; Simard et al., 2011). The use of longer time records of GEDI data to enhance training and compensating biases of h_{veg} models could help to reduce uncertainties (Lang et al., 2022).

Second, we cannot exclude that the differences between L-VOD (from MT-DCA algorithm) and X- and Ku-VOD (from VODCA algorithm) are partially due to specifications in the algorithms. In addition, note that the VOD products applied have different temporal and spatial resolutions. Moreover, Ku-band is limited to July 2017. The use of the same satellite, algorithm, time period and temporal resolution would be the ideal case for comparing VOD products at multiple frequencies. This will be possible with the upcoming Copernicus Imaging Radiometer mission (CIMR; Donlon, 2023), planned to be launched in 2027.

Third, the active microwave part included in this study is the Sentinel-1C-band radar backscatter, which guarantees regular temporal resolution (of ~6 days from 2017 to 2022) with an open-access data policy. The application of other frequencies matching the VOD ones used here is hampered by the restricted data availability and/or the low temporal resolution of radar missions operating at L-, X- or Ku-bands. Although using the same frequency in radar and radiometer data would be ideal in our algorithm, we note that using normalized radar backscatter (σ_{norm}) limits the impact of the variations in absolute values due to differences among frequencies. Still, a main limitation of the current research is the usage of a constant penetration depth to account for vegetation structure and density, while using a variable sensing depth for the microwave attenuation. Further research should be conducted with future radar missions to overcome this limitation. In particular, the launch of the NASA-ISRO SAR (NISAR) mission (Kellogg et al., 2020), planned for 2024, and of the Copernicus L-band Synthetic Aperture Radar (ROSE-L; Pierdicca et al., 2019), planned for 2028, should provide open data of radar backscatter at L-band.

5. Conclusions

In this study, we have retrieved vegetation moisture information using a satellite multi-sensor synergy in the Western United States. An attenuation-based, semi-physical retrieval algorithm is proposed to disentangle the water component from the structure and biomass components of the VOD. Passive microwave VOD retrievals from SMAP and AMSR2, radar backscatter data from Sentinel-1, and canopy height information based on GEDI and Sentinel-2, are used as inputs. As a result, LFMC estimates are obtained at three microwave frequencies: L-, X- and Ku-bands.

Spatio-temporal dynamics of the LFMC estimates at X- and Ku-bands are consistent with climate and seasonal precipitation patterns. Retrievals show similar dynamic range and average values regardless of the frequency, the vegetation density, the canopy height, and the land cover. This demonstrates that the retrieval method isolates the water component from the biomass/structure influences also contained in the VOD signal.

Comparison of LFMC retrievals with *in situ* LFMC measurements shows good agreement at X- and Ku-bands, both at regional scale ($r >$ 0.6; RMSE and bias <30%) and for specific pixel-scale comparisons (in most cases, r is between 0.50 and 0.94; RMSE and biases <40%). This performance is also obtained over forests and shrubs separately but decreases for grasslands. The latter is probably due to the lack of time-dynamic canopy height information and due to the limitations of *in situ* data in grass sites. At L-band, the performance is lower ($r = 0.37$) with no correlation in forests and a moderate correlation in shrublands ($r = 0.46$). This is because of the mismatch between the entire canopy depth sensed at L-band, and the fact that *in situ* LFMC samples are taken only from the top leaves and twigs of the canopy. We suggest that L-band LFMC retrievals would perform well against vertically stratified *in situ* LFMC measurements from top to down canopy layers, according to results and literature.

By isolating the vegetation moisture information from VOD at three frequencies in a large study region, the proposed approach paves the way for future global LFMC retrievals for multiple vegetation canopy layers. In that sense, further research will be conducted to evaluate the global applicability of the approach and its capacity to disentangle the water component of VOD in heterogeneous pixels and in grassland-dominated regions. This VOD decomposition algorithm will be applicable with future sensor synergies using consistent radiometer-radar frequencies from CIMR, ROSE-L, or Sentinel-1 data, together with time-dynamic vegetation height data from GEDI. The multi-layer retrievals should be accompanied by a relevant effort for an enlarged LFMC *in situ* sampling strategy including measurements from both the leaves and the woody components of vegetation. Then, the application and validation of LFMC products would qualify for higher user readiness levels for applications such as fire risk or tree mortality assessment, crop yield estimation, and vegetation stress monitoring.

CRediT authorship contribution statement

David Chaparro: Conceptualization, Data curation, Formal analysis, Funding acquisition, Investigation, Validation, Writing – original draft, Writing – review & editing. **Thomas Jagdhuber:** Conceptualization, Data curation, Formal analysis, Funding acquisition, Supervision, Writing – original draft, Writing – review & editing. **María Piles:** Conceptualization, Data curation, Formal analysis, Supervision, Writing – original draft, Writing – review & editing. **François Jonard:** Conceptualization, Formal analysis, Supervision, Writing – original draft, Writing – review & editing. **Anke Fluhrer:** Conceptualization, Writing – original draft, Writing – review & editing. **Mercè Vall-llossera:** Conceptualization, Writing – original draft, Funding acquisition. **Adriano Camps:** Conceptualization, Writing – original draft, Writing – review & editing. **Carlos López-Martínez:** Conceptualization, Writing – original draft, Writing – review & editing. **Roberto Fernández-Morán:** Data curation, Writing – original draft. **Martin Baur:** Conceptualization, Writing – original draft. **Andrew F. Feldman:** Writing – original draft, Writing – review & editing. **Anita Fink:** Conceptualization. **Dara Entekhabi:** Conceptualization, Writing – original draft, Supervision.

Declaration of competing interest

The authors declare that they have no known competing financial interests or personal relationships that could have appeared to influence the work reported in this paper.

## Data availability

Acknowledgements

Appendix A. Calibration of *a* and *b* parameters using the VOD-to-vegetation height relationship

In the calibration process, linear regressions between VOD and h_{veg} are performed for each frequency and σ_{norm} bin (outliers are screened by using five times the Cook's distance in the regression). The resulting coefficients of each regression are used to predict VOD values from h_{veg}. Then, accounting for the assumption that the regression line shows average moisture conditions, a value of $m_g = 0.5$ kg·kg^{-1} is embedded in the algorithm. This leaves only two unknowns (*a* and *b*) which are solved because m_g, VOD and h_{veg} values are known.

In this process, the first assumption states that points laying exactly over the regression line correspond to average vegetation moisture because this line represents the average vegetation conditions. This is tested with a sensitivity analysis which assigns m_g values different than 0.5 kg·kg^{-1} (*i.e.*, different to the average) to the VOD-h_{veg} regression line. These values are the minimum and maximum m_g according to the literature review presented in Table S1 (0.42 kg·kg^{-1} and 0.57 kg·kg^{-1}, respectively). For completeness, lower (0.35 kg·kg^{-1}) and higher (0.65 kg·kg^{-1}) values are also tested. Results of the comparisons between estimates and *in situ* measurements show larger biases than those found for LFMC estimates using 0.5 kg·kg^{-1} as a reference value.

A second assumption is made, which states that the average $m_g = 0.5$ kg·kg^{-1}. This is confirmed by the literature review presented in Table S1. There, the median vegetation moisture is close to 0.5 kg·kg^{-1} for most land covers. Also, Table S1 shows that the average m_g from *in situ* measurements derived from Yebra et al. (2019) for each land cover class is close to 0.5 kg·kg^{-1}. Note that, because this dataset is also used in the comparison between m_g estimates and *in situ* m_g in our study area (Section 2.2.4), only data from outside the study region has been used to compute the averages reported in Table S1, to ensure that the calibration and comparison processes are statistically fully independent.
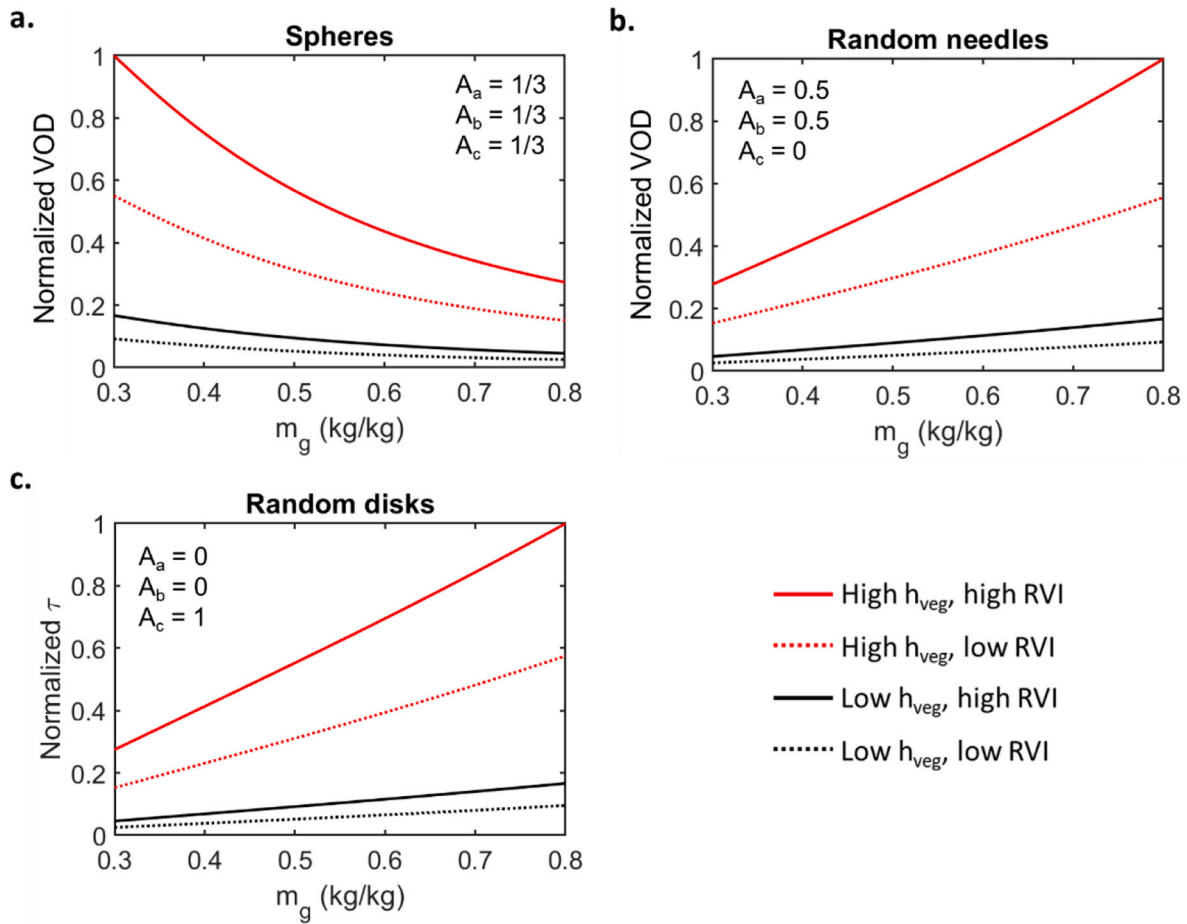
Fig. A1. (a) Spheres, (b) random needles and (c) random disks models for the shapes of inclusions are plotted for different conditions: h_{veg} (high = 30 m.; low = 5 m.) and σ_{norm} (high = 0.20; low = 0.11). VOD is normalized (divided by maximum VOD) to make all models comparable in magnitude. A_a, A_b and A_c the depolarization factors, which are computed using normalized semi-axes of the spheroids (De Loor, 1968; Ulaby et al., 2014).

Appendix B. Two-phase dielectric mixing models of vegetation and their shapes of inclusions

The two-phase dielectric mixing models for vegetation, used to calculate ε_{can}, depend on the assumed shapes of inclusions. The assumptions proposed in Ulaby et al. (2014) have been tested in this work: spheres ($A_a = A_b = A_c = \frac{1}{3}$), random needles ($A_a = A_b = 0.5; A_c = 0$) and random disks ($A_a = A_b = 0; A_c = 1$). Fig. A1 plots the relationships between VOD and m_g for each assumption. Fig. A1a shows the behavior of the model using the spheres approximation, where the attenuation (VOD) increases when the plants are drier and decreases for wetter plants. This is a non-physical behavior because more water in vegetation should result in higher microwave attenuation. Therefore, the spheres approach is discarded. Instead, the random needles and random disks approaches show how increasing attenuation (VOD) is linked to increasing vegetation moisture, which makes physical sense. Both approaches are almost equal when VOD is normalized (Fig. A1b and c) meaning that the model is applicable independently of the

shapes of leaves in vegetation. The random needles approach is chosen as it has been used in previous literature (Meyer et al., 2019).

Appendix C. Supplementary data

Supplementary data to this article can be found online at https://doi.org/10.1016/j.rse.2024.113993.

References

Baccini, A., Laporte, N., Goetz, S.J., Sun, M., Dong, H., 2008. A first map of tropical Africa's above-ground biomass derived from satellite imagery. Environ. Res. Lett. 3 (4), 045011.

Bohlinger, P., Sorteberg, A., Sodemann, H., 2017. Synoptic conditions and moisture sources actuating extreme precipitation in Nepal. J. Geophys. Res. Atmos. 122 (23).

Bouvet, A., Mermoz, S., Le Toan, T., Villard, L., Mathieu, R., Naidoo, L., Asner, G.P., 2018. An above-ground biomass map of African savannahs and woodlands at 25 m resolution derived from ALOS PALSAR. Remote Sens. Environ. 206, 156–173.

Bueso, D., Piles, M., Ciais, P., Wigneron, J.P., Moreno-Martínez, Á., Camps-Valls, G., 2023. Soil and vegetation water content identify the main terrestrial ecosystem changes. Natl. Sci. Rev. 10 (5) (nwad026).

Chaparro, D., Vayreda, J., Vall-Llossera, M., Banqué, M., Piles, M., Camps, A., Martinez-Vilalta, J., 2016. The role of climatic anomalies and soil moisture in the decline of drought-prone forests. IEEE J. Select. Top. Appl. Earth Observ. Remote Sens. 10 (2), 503–514.

Chaparro, D., Duveiller, G., Piles, M., Cescatti, A., Vall-Llossera, M., Camps, A., Entekhabi, D., 2019. Sensitivity of L-band vegetation optical depth to carbon stocks in tropical forests: a comparison to higher frequencies and optical indices. Remote Sens. Environ. 232, 111303.

Chaparro, D., Jagdhuber, T., Piles, M., Entekhabi, D., Jonard, F., Fluhrer, A., Camps, A., 2021. Global L-band vegetation volume fraction estimates for modeling vegetation optical depth. In: 2021 IEEE International Geoscience and Remote Sensing Symposium IGARSS. IEEE, pp. 6399–6402. July.

Chaparro, D., Feldman, A.F., Chaubell, M.J., Yueh, S.H., Entekhabi, D., 2022. Robustness of vegetation optical depth retrievals based on L-band global radiometry. IEEE Trans. Geosci. Remote Sens. 60, 1–17.

Choudhury, B.J., Kerr, Y.H., Njoku, E.G., Pampaloni, P. (Eds.), 1994. Passive Microwave Remote Sensing of Land-Atmosphere Interactions, ESA/NASA International Workshop. VSP.

Chuvieco, E., Riaño, D., Aguado, I., Cocero, D., 2002. Estimation of fuel moisture content from multitemporal analysis of Landsat thematic mapper reflectance data: applications in fire danger assessment. Int. J. Remote Sens. 23 (11), 2145–2162.

Chuvieco, E., Cocero, D., Riaño, D., Martin, P., Martinez Vega, J., De La Riva, J., Perez, F., 2004. Combining NDVI and surface temperature for the estimation of live fuel moisture content in forest fire danger rating. Remote Sens. Environ. 92 (3), 322–331.

Chuvieco, E., Aguado, I., Yebra, M., Nieto, H., Salas, J., Martín, Zamora, R., 2010. Development of a framework for fire risk assessment using remote sensing and geographic information system technologies. Ecol. Model. 221 (1), 46–58.

Cloude, S.R., 2010. Polarization Application in Remote Sensing. Oxford University Press, Oxford.

Couvreur, V., Ledder, G., Manzoni, S., Way, D.A., Muller, E.B., Russo, S.E., 2018. Water transport through tall trees: a vertically explicit, analytical model of xylem hydraulic conductance in stems. Plant Cell Environ. 41 (8), 1821–1839.

Das, N., Entekhabi, D., Dunbar, S., Chaubell, J., Colliander, A., Yueh, S., Thibeault, M., 2019. The SMAP and Copernicus sentinel 1A/B microwave active-passive high-resolution surface soil moisture product. Remote Sens. Environ. 233, 111380.

Das, N., Entekhabi, D., Dunbar, R.S., Kim, S., Yueh, S., Colliander, A., Cosh, M., 2020. SMAP/Sentinel-1 L2 Radiometer/Radar 30-Second Scene 3 Km EASE-Grid Soil Moisture, Version 3. NASA National Snow and Ice Data Center Distributed Active Archive Center, Boulder, Colorado USA. https://doi.org/10.5067/ASB0EQO2LYJV. [20-04-2022].

De Loor, G.P., 1968. Dielectric properties of heterogeneous mixtures containing water. J. Microwave Power 3, 67–73.

Dennison, P.E., Roberts, D.A., Peterson, S.H., Rechel, J., 2005. Use of normalized difference water index for monitoring live fuel moisture. Int. J. Remote Sens. 26 (5), 1035–1042.

Donlon, C.J., 2023. The Copernicus Imaging Microwave Radiometer (CIMR) Mission Requirements Document v5. 0. ESA, Paris, France. https://cimr.eu/mrd_v5.

Duché, Y., Savazzi, R., Toutchkov, M., Cabanne, E., 2017. Multisite and multispecies live fuel moisture content (LFMC) series in the French Mediterranean since 1996 [data set]. Zenodo. https://doi.org/10.5281/zenodo.162978.

Entekhabi, D., Njoku, E.G., O'Neill, P.E., Kellogg, K.H., Crow, W.T., Edelstein, W.N., Van Zyl, J., 2010. The soil moisture active passive (SMAP) mission. Proc. IEEE 98 (5), 704–716. https://doi.org/10.1109/JPROC.2010.2043918.

Fan, L., Wigneron, J.-P., Xiao, Q., Al-Yaari, A., Wen, J., Martin-StPaul, N., Kerr, Y.H., 2018. Evaluation of microwave remote sensing for monitoring live fuel moisture content in the Mediterranean region. Remote Sens. Environ. 205, 210–223.

Feldman, A.F., Akbar, R., Entekhabi, D., 2018. Characterization of higher-order scattering from vegetation with SMAP measurements. Remote Sens. Environ. 219, 324–338.

Feldman, A., Konings, A., Piles, M., Entekhabi, D., 2021. The multi-temporal dual channel algorithm (MT-DCA) (version 5) [data set]. Zenodo. https://doi.org/10.5281/zenodo.5579549.

Fink, A., Jagdhuber, T., Piles, M., Grant, J., Baur, M., Link, M., Entekhabi, D., 2018. Estimating gravimetric moisture of vegetation using an attenuation-based multi-sensor approach. In: IGARSS 2018–2018 IEEE International Geoscience and Remote Sensing Symposium, pp. 353–356.

Forkel, M., Schmidt, L., Zotta, R.-M., Dorigo, W., Yebra, M., 2022. Leaf moisture content (live-fuel moisture content) at global scale from passive microwave satellite observations of vegetation optical depth (VOD2LFMC) (version 01) [data set]. Zenodo. https://doi.org/10.5281/zenodo.6545571.

Forkel, M., Schmidt, L., Zotta, R.-M., Dorigo, W., Yebra, M., 2023. Estimating leaf moisture content at global scale from passive microwave satellite observations of vegetation optical depth. Hydrol. Earth Syst. Sci. 27 (1), 39–68.

Gentine, P., Green, J.K., Guérin, M., Humphrey, V., Seneviratne, S.I., Zhang, Y., Zhou, S., 2019. Coupling between the terrestrial carbon and water cycles—a review. Environ. Res. Lett. 14 (8), 083003.

Grant, J., Wigneron, J.-P., Williams, M., Scholze, M., Kerr, Y., 2014. Working towards a global-scale vegetation water product from SMOS optical depth. In: 2014 IEEE Geoscience and Remote Sensing Symposium, pp. 286–289.

Grossiord, C., Buckley, T.N., Cernusak, L.A., Novick, K.A., Poulter, B., Siegwolf, R.T.W., McDowell, N.G., 2020. Plant responses to rising vapor pressure deficit. New Phytol. 226 (6), 1550–1566.

Holtzman, N.M., Anderegg, L.D., Kraatz, S., Mavrovic, A., Sonnentag, O., Pappas, C., Konings, A.G., 2021. L-band vegetation optical depth as an indicator of plant water potential in a temperate deciduous forest stand. Biogeosciences 18 (2), 739–753.

Imaoka, K., Kachi, M., Fujii, H., Murakami, H., Hori, M., Ono, A., Shimoda, H., 2010. Global change observation Mission (GCOM) for monitoring carbon, water cycles, and climate change. Proc. IEEE 98 (5), 717–734.

Jackson, T.J., Schmugge, T.J., 1991. Vegetation effects on the microwave emission of soils. Remote Sens. Environ. 36 (3), 203–212.

Jagdhuber, T., Jonard, F., Fluhrer, A., Chaparro, D., Baur, M.J., Meyer, T., Piles, M., 2022. Toward estimation of seasonal water dynamics of winter wheat from ground-based L-band radiometry: a concept study. Biogeosciences 19 (8), 2273–2294.

Jia, S., Kim, S.H., Nghiem, S.V., Kafatos, M., 2019. Estimating live fuel moisture using SMAP L-band radiometer soil moisture for Southern California, USA. Remote Sens. 11 (13), 1575.

Jonard, F., Feldman, A.F., Short Gianotti, D.J., Entekhabi, D., 2022. Observed water and light limitation across global ecosystems. Biogeosciences 19 (23), 5575–5590.

Kawanishi, T., Sezai, T., Ito, Y., Imaoka, K., Takeshima, T., Ishido, Y., Spencer, R.W., 2003. The advanced microwave scanning radiometer for the earth observing system (AMSR-E), NASDA's contribution to the EOS for global energy and water cycle studies. IEEE Trans. Geosci. Remote Sens. 41 (2), 184–194.

Kellogg, K., Hoffman, P., Standley, S., Shaffer, S., Rosen, P., Edelstein, W., Sarma, C.V.H. S., 2020. NASA-ISRO synthetic aperture radar (NISAR) mission. In: In 2020 IEEE Aerospace Conference. IEEE, pp. 1–21. March.

Kerr, Y.H., Waldteufel, P., Wigneron, J.-P., Delwart, S., Cabot, F., Boutin, J., Mecklenburg, S., 2010. The SMOS Mission: new tool for monitoring key elements of the global water cycle. Proc. IEEE 98 (5), 666–687.

Kim, Y., van Zyl, J., 2000, July. On the relationship between polarimetric parameters. In: IGARSS 2000. IEEE 2000 International Geoscience and Remote Sensing Symposium. Taking the Pulse of the Planet: The Role of Remote Sensing in Managing the Environment. Proceedings (Cat. No. 00CH37120), 3. IEEE, pp. 1298–1300.

Koike, T., Njoku, E., Jackson, T.J., Paloscia, S., 2000, July. Soil moisture algorithm development and validation for the ADEOS-II/AMSR. In: IGARSS 2000. IEEE 2000 International Geoscience and Remote Sensing Symposium. Taking the Pulse of the Planet: The Role of Remote Sensing in Managing the Environment. Proceedings (Cat. No. 00CH37120), 3. IEEE, pp. 1253–1255.

Konings, A.G., Gentine, P., 2017. Global variations in ecosystem-scale isohydricity. Glob. Chang. Biol. 23 (2), 891–905.

Konings, A.G., Piles, M., Rötzer, K., McColl, K.A., Chan, S.K., Entekhabi, D., 2016. Vegetation optical depth and scattering albedo retrieval using time series of dual-polarized L-band radiometer observations. Remote Sens. Environ. 172, 178–189.

Konings, A.G., Rao, K., Steele-Dunne, S.C., 2019. Macro to micro: microwave remote sensing of plant water content for physiology and ecology. New Phytol. 223 (3), 1166–1172.

Konings, A.G., Saatchi, S.S., Frankenberg, C., Keller, M., Leshyk, V., Anderegg, W.R., Zuidema, P.A., 2021. Detecting forest response to droughts with global observations of vegetation water content. Glob. Chang. Biol. 27 (23), 6005–6024.

Lang, N., Jetz, W., Schindler, K., Wegner, J.D., 2022. A High-Resolution Canopy Height Model of the Earth. arXiv preprint. arXiv:2204.08322.

Li, Z., Zeng, J., Chen, Q., Bi, H., 2014. The measurement and model construction of complex permittivity of vegetation. Sci. China Earth Sci. 57 (4), 729–740.

Li, X., Wigneron, J.P., Frappart, F., Fan, L., Ciais, P., Fensholt, R., Moisy, C., 2021. Global-scale assessment and inter-comparison of recently developed/reprocessed microwave satellite vegetation optical depth products. Remote Sens. Environ. 253, 112208.

Liu, Y.Y., Van Dijk, A.I., De Jeu, R.A., Canadell, J.G., McCabe, M.F., Evans, J.P., Wang, G., 2015. Recent reversal in loss of global terrestrial biomass. Nat. Clim. Chang. 5 (5), 470–474.

Mandal, D., Kumar, V., Ratha, D., Dey, S., Bhattacharya, A., Lopez-Sanchez, J.M., Rao, Y. S., 2020. Dual polarimetric radar vegetation index for crop growth monitoring using sentinel-1 SAR data. Remote Sens. Environ. 247, 111954.

Martinez-Vilalta, J., Anderegg, W.R.L., Sapes, G., Sala, A., 2019. Greater focus on water pools may improve our ability to understand and anticipate drought-induced mortality in plants. New Phytol. 223 (1), 22–32.

Matzler, C., 1994. Microwave (1-100 GHz) dielectric model of leaves. IEEE Trans. Geosci. Remote Sens. 32 (4), 947–949.

Meyer, T., Jagdhuber, T., Piles, M., Fink, A., Grant, J., Vereecken, H., Jonard, F., 2019. Estimating gravimetric water content of a winter wheat field from L-band vegetation optical depth. Remote Sens. 11 (20), 2353.

Miralles, D.G., Gentine, P., Seneviratne, S.I., Teuling, A.J., 2019. Land–atmospheric feedbacks during droughts and heatwaves: state of the science and current challenges. Ann. N. Y. Acad. Sci. 1436 (1), 19–35.

Mo, T., Choudhury, B.J., Schmugge, T.J., Wang, J.R., Jackson, T.J., 1982. A model for microwave emission from vegetation-covered fields. J. Geophys. Res. Oceans 87 (C13), 11229–11237.

Moesinger, L., Dorigo, W., de Jeu, R., van der Schalie, R., Scanlon, T., Teubner, I., Forkel, M., 2020. The global long-term microwave vegetation optical depth climate archive (VODCA). Earth Syst. Sci. Data 12 (1), 177–196.

Myoung, B., Kim, S., Nghiem, S., Jia, S., Whitney, K., Kafatos, M., 2018. Estimating live fuel moisture from MODIS satellite data for wildfire danger assessment in Southern California USA. Remote Sens. 10 (2), 87.

Olivares-Cabello, C., Chaparro, D., Vall-llossera, M., Camps, A., López-Martínez, C., 2022. Global unsupervised assessment of multifrequency vegetation optical depth sensitivity to vegetation cover. IEEE J. Select. Top. Appl. Earth Observ. Remote Sens. 16, 538–552.

O'Neill, P.E., Chan, S., Njoku, E.G., Jackson, T., Bindlish, R., Chaubell, J., 2020. SMAP Enhanced L3 Radiometer Global Daily 9 Km EASE-Grid Soil Moisture, Version 4 [Data Set]. NASA National Snow and Ice Data Center Distributed Active Archive Center, Boulder, Colorado USA. https://doi.org/10.5067/NJ34TQ2LFE90. Date Accessed 06-06-2023.

Pierdicca, N., Davidson, M., Chini, M., Dierking, W., Djavidnia, S., Haarpaintner, J., Su, B., 2019. The copernicus L-band SAR mission ROSE-L (radar observing system for Europe) (conference presentation). In: In Active and Passive Microwave Remote Sensing for Environmental Monitoring III, vol. 11154. SPIE, p. 111540E. October.

Piles, M., Camps, A., Vall-Llossera, M., Corbella, I., Panciera, R., Rudiger, C., Walker, J., 2011. Downscaling SMOS-derived soil moisture using MODIS visible/infrared data. IEEE Trans. Geosci. Remote Sens. 49 (9), 3156–3166.

Potapov, P., Li, X., Hernandez-Serna, A., Tyukavina, A., Hansen, M.C., Kommareddy, A., Hofton, M., 2021. Mapping global forest canopy height through integration of GEDI and Landsat data. Remote Sens. Environ. 253, 112165.

Rao, K., Anderegg, W.R., Sala, A., Martínez-Vilalta, J., Konings, A.G., 2019. Satellite-based vegetation optical depth as an indicator of drought-driven tree mortality. Remote Sens. Environ. 227, 125–136.

Rao, K., Williams, A.P., Flefil, J.F., Konings, A.G., 2020. SAR-enhanced mapping of live fuel moisture content. Remote Sens. Environ. 245, 111797.

Rigden, A.J., Mueller, N.D., Holbrook, N.M., Pillai, N., Huybers, P., 2020. Combined influence of soil moisture and atmospheric evaporative demand is important for accurately predicting US maize yields. Nat. Food 1 (2), 127–133.

Rodríguez-Fernández, N.J., Mialon, A., Mermoz, S., Bouvet, A., Richaume, P., Al Bitar, A., Wigneron, J.P., 2018. An evaluation of SMOS L-band vegetation optical depth (L-VOD) data sets: high sensitivity of L-VOD to above-ground biomass in Africa. Biogeosciences 15 (14), 4627–4645.

Santi, E., Paloscia, S., Pampaloni, P., Pettinato, S., Nomaki, T., Seki, M., Maeda, T., 2017. Vegetation water content retrieval by means of multifrequency microwave

acquisitions from AMSR2. IEEE J. Select. Top. Appl. Earth Observ. Remote Sens. 10 (9), 3861–3873.

Schmidt, L., Forkel, M., Zotta, R.M., Scherrer, S., Dorigo, W.A., Kuhn-Régnier, A., Yebra, M., 2023. Assessing the sensitivity of multi-frequency passive microwave vegetation optical depth to vegetation properties. Biogeosciences 20 (5), 1027–1046.

Schmugge, T.J., Jackson, T.J., 1992. A dielectric model of the vegetation effects on the microwave emission from soils. IEEE Trans. Geosci. Remote Sens. 30 (4), 757–760.

Simard, M., Pinto, N., Fisher, J.B., Baccini, A., 2011. Mapping forest canopy height globally with spaceborne lidar. J. Geophys. Res. Biogeosci. 116 (G4).

Szigarski, C., Jagdhuber, T., Baur, M., Thiel, C., Parrens, M., Wigneron, J.-P., Entekhabi, D., 2018. Analysis of the radar vegetation index and potential improvements. Remote Sens. 10 (11), 1776.

Teubner, I.E., Forkel, M., Jung, M., Liu, Y.Y., Miralles, D.G., Parinussa, R., Dorigo, W.A., 2018. Assessing the relationship between microwave vegetation optical depth and gross primary production. Int. J. Appl. Earth Obs. Geoinf. 65, 79–91.

Togliatti, K., Hartman, T., Walker, V.A., Arkebauer, T.J., Suyker, A.E., VanLoocke, A., Hornbuckle, B.K., 2019. Satellite L–band vegetation optical depth is directly proportional to crop water in the US Corn Belt. Remote Sens. Environ. 233, 111378.

Torres, R., Snoeij, P., Geudtner, D., Bibby, D., Davidson, M., Attema, E., Rostan, F., 2012. GMES Sentinel-1 mission. Remote Sens. Environ. 120, 9–24.

Ulaby, F., El-Rayes, M., 1987. Microwave dielectric spectrum of vegetation - part II: dual-dispersion model. IEEE Trans. Geosci. Remote Sens. GE-25 (5), 550–557.

Ulaby, F.T., Razani, M., Dobson, M.C., 1983. Effects of vegetation cover on the microwave radiometric sensitivity to soil moisture. IEEE Trans. Geosci. Remote Sens. GE-21 (1), 51–61.

Ulaby, F.T., Long, D.G., Blackwell, W.J., Elachi, C., Fung, A.K., Ruf, C., Sarabandi, K., Zebker, H.A., Van Zyl, J., 2014. Microwave Radar and Radiometric Remote Sensing. University of Michigan Press, Artech House, MI, USA.

Wigneron, J.P., Kerr, Y., Chanzy, A., Jin, Y.Q., 1993. Inversion of surface parameters from passive microwave measurements over a soybean field. Remote Sens. Environ. 46 (1), 61–72.

Wright, J.S., Fu, R., Worden, J.R., Chakraborty, S., Clinton, N.E., Risi, Y., Yin, L., 2017. Rainforest-initiated wet season onset over the southern Amazon. Proc. Natl. Acad. Sci. 114 (32), 8481–8486.

Xu, X., Konings, A.G., Longo, M., Feldman, A., Xu, L., Saatchi, S., Moorcroft, P., 2021. Leaf surface water, not plant water stress, drives diurnal variation in tropical forest canopy water content. New Phytol. 231 (1), 122–136.

Yang, H., Ciais, P., Frappart, F., Li, X., Brandt, M., Fensholt, R., Wigneron, J.P., 2023. Global increase in biomass carbon stock dominated by growth of northern young forests over past decade. Nat. Geosci. 16, 886–892.

Yebra, M., Chuvieco, E., 2009. Linking ecological information and radiative transfer models to estimate fuel moisture content in the Mediterranean region of Spain: solving the ill-posed inverse problem. Remote Sens. Environ. 113 (11), 2403–2411.

Yebra, M., Quan, X., Riaño, D., Rozas Larraondo, P., Van Dijk, A.I.J.M., Cary, G.J., 2018. A fuel moisture content and flammability monitoring methodology for continental Australia based on optical remote sensing. Remote Sens. Environ. 212, 260–272.

Yebra, M., Scortechini, G., Badi, A., Beget, M.E., Boer, M.M., Bradstock, R., Ustin, S., 2019. Globe-LFMC, a global plant water status database for vegetation ecophysiology and wildfire applications. Sci. Data 6 (1), 155.

Yu, Y., Notaro, M., 2020. Observed land surface feedbacks on the Australian monsoon system. Clim. Dyn. 54 (5–6), 3021–3040.

Zemp, D.C., Schleussner, C.-F., Barbosa, H.M.J., van der Ent, R.J., Donges, J.F., Heinke, J., Rammig, A., 2014. On the importance of cascading moisture recycling in South America. Atmos. Chem. Phys. 14 (23), 13337–13359.

Zweifel, R., Item, H., Häsler, R., 2001. Link between diurnal stem radius changes and tree water relations. Tree Physiol. 21 (12–13), 869–877.